

# Solving Time-Fractional Partial Integro-Differential Equations Using Tensor Neural Networks

Zhongshuo Lin\*, Qingkui Ma†, Hehu Xie‡ and Xiaobo Yin§

## Abstract

In this paper, we propose a novel machine learning method based on adaptive tensor neural network subspace to solve linear time-fractional diffusion-wave equations and non-linear time-fractional partial integro-differential equations. In this framework, the tensor neural network and Gauss-Jacobi quadrature are effectively combined to construct a universal numerical scheme for the temporal Caputo derivative with orders spanning  $(0, 1)$  and  $(1, 2)$ . Specifically, in order to effectively utilize Gauss-Jacobi quadrature to discretize Caputo derivatives, we design the tensor neural network function multiplied by the function  $t^\mu$  where the power  $\mu$  is selected according to the parameters of the equations at hand. Finally, some numerical examples are provided to validate the efficiency and accuracy of the proposed tensor neural network-based machine learning method.

**Keywords.** time-fractional partial integro-differential equations, tensor neural network, adaptive subspace method, Gauss-Jacobi quadrature, high-accuracy

## 1 Introduction

Fractional partial differential equations (FPDEs) differ from traditional differential equations in their nonlocal nature induced by fractional differential operators. This nonlocality enables FPDEs to effectively capture memory effects and hereditary characteristics which are widely observed in real-world phenomena[18, 22, 10]. Due to these properties, FPDEs demonstrate significant potential for applications in diverse fields [29], including anomalous diffusion, fluid mechanics, electromagnetism, statistical modeling, and signal processing. For example, the time-fractional diffusion wave equation can simulate complex diffusion and wave phenomena in diverse applications such as fluid dynamics, petroleum reservoir engineering, and anomalous transport processes[6, 9, 28, 31].

However, solving FPDEs faces a huge challenge. Analytical solutions are often intractable and difficult to derive, especially for problems involving complex geometries, boundary conditions, or nonlinear terms, and even when available, frequently involve complex special functions,

\*LSEC, Academy of Mathematics and Systems Science, Chinese Academy of Sciences, No.55, Zhongguancun Donglu, Beijing 100190, China, and School of Mathematical Sciences, University of Chinese Academy of Sciences, Beijing, 100049 (linzhongshuo@lsec.cc.ac.cn).

†School of Mathematics and Statistics & Hubei Key Laboratory of Mathematical Sciences, Central China Normal University, Wuhan 430079, China., \*Corresponding author (maqingkui@mails.ccnu.edu.cn)

‡LSEC, Academy of Mathematics and Systems Science, Chinese Academy of Sciences, No.55, Zhongguancun Donglu, Beijing 100190, China, and School of Mathematical Sciences, University of Chinese Academy of Sciences, Beijing, 100049, China (hhxie@lsec.cc.ac.cn).

§School of Mathematics and Statistics & Key Laboratory of Nonlinear Analysis & Applications (Ministry of Education), Central China Normal University, Wuhan 430079, China (yinxb@mail.ccnu.edu.cn), the research is supported by National Natural Science Foundation of China (NSFC 12471380)

such as Mittag-Leffler functions, H-functions, and Wright functions [1]. To address these challenges, various numerical methods have been developed to solve FPDEs, e.g., the finite difference method [13, 27, 29], finite element method [10, 39, 42], spectral method [3, 4], wavelet method [7, 19], Laplace transform method [26], matrix method [30], and domain decomposition method [20, 21, 24]. These traditional approaches have successfully tackled fractional derivatives to some extent, laying a solid foundation for the further development of numerical methods for FPDEs.

While these achievements are encouraging, traditional numerical techniques often struggle to efficiently handle the nonlocal nature of fractional derivatives, frequently resulting in increased computational complexity, memory consumption and reduced accuracy. To fully exploit the potential of FPDEs in various fields, it is crucial to develop more efficient and accurate numerical methods. In recent years, neural networks have become an active research focus across various fields of science and engineering. Thanks to their powerful approximation capabilities, neural networks have demonstrated exceptional performance in solving complex problems. Many neural-network-based numerical methods have been proposed to solve partial differential equations. For instance, Lagaris et al. [14] are early pioneers in applying artificial neural networks to solve differential equations, constructing approximate solutions for initial and boundary value problems. Raissi et al. [23] introduce the physics-informed neural networks (PINNs), a novel general-purpose function approximator that efficiently encodes physical information into the loss function of the neural network for guiding training. The forward and inverse problems of partial differential equations were successfully solved within a given data set. To solve space-time fractional advection-diffusion equations, fractional physics-informed neural networks (fPINNs) have been proposed [22]. In fPINNs, the L1 scheme is employed to approximate the temporal Caputo fractional derivative, while the shifted vector Grünwald-Letnikov scheme is used to discretize the spatial fractional Laplacian. Ma et al. introduce Bi-orthogonal fPINN [17], which combines biorthogonal constraints with PINNs to solve random FPDEs. Wang and Karniadakis [32] propose a general (quasi) Monte Carlo PINN to solve FPDEs on irregular domains. Ma et al. [18] establish a physical model-driven neural network to solve FPDEs, which effectively combines deep neural networks (DNNs) with interpolation approximation of fractional derivatives. Ren et al. [25] propose an improved fractional physics-informed neural networks (IFPINNs), which enhance the capabilities of traditional PINNs by incorporating nonlinear weight propagation to solve FPDEs with high oscillations or singular perturbations. Zhang et al. [40] establish an adaptive loss weighting auxiliary output fractional physics-informed neural networks (AWAO-fPINNs) to solve time-fractional partial integral-differential equations (TFPIDEs). Zhang et al. [41] proposed spectral-fPINNs, a framework combining spectral methods with physics-informed neural networks that employs Jacobi polynomials for global discretization of FPDEs, addressing challenges in solving both forward and inverse problems involving fractional-order operators.

Recently, Wang et al. [15, 16, 34, 35, 36] propose a type of tensor neural network (TNN) and corresponding machine learning method to solve high-dimensional problems. The special structure of TNN transforms the high-dimensional integration of TNN functions involved in the loss functions to one-dimensional integration, which can be computed using the classical quadrature schemes with high accuracy and efficiency. The TNN-based machine learning method has already been used to solve high-dimensional eigenvalue problems and boundary value problems by Ritz-type loss functions [34]. Furthermore, in [36], the multi-eigenpairs are computed by a machine learning method which combines TNN and Rayleigh-Ritz process. With the help of TNN, a posterior error estimator can be used as a loss function in machine learning methods to solve high-dimensional boundary value problems and eigenvalue problems [35]. TNN has also been utilized to solve the Schrödinger equation for 20,000-dimensional coupled harmonic oscillators [5], high-dimensional Fokker-Planck equations [33], and high-dimensional time-dependent

problems[12].

In this paper, we aim to design efficient machine learning method for solving the following (linear or nonlinear) TFPIDEs with single-term or multi-term time fractional derivative: Find  $u(\mathbf{x}, t)$  such that

$$\begin{cases} Lu(\mathbf{x}, t) = f(\mathbf{x}, t, u(\mathbf{x}, t)), (\mathbf{x}, t) \in \Omega \times (0, T], \\ u(\mathbf{x}, t) = g(\mathbf{x}, t), (\mathbf{x}, t) \in \partial\Omega \times (0, T], \\ u(\mathbf{x}, 0) = s(\mathbf{x}), \mathbf{x} \in \Omega, \end{cases} \quad (1.1)$$

where the domain  $\Omega$  is defined as  $(a_1, b_1) \times \cdots \times (a_d, b_d)$ . The function  $f(\mathbf{x}, t, u(\mathbf{x}, t))$  is linearly or nonlinearly dependent on  $u(\mathbf{x}, t)$ . For the nonlinear case, we consider the form  $f(\mathbf{x}, t, u) = h(\mathbf{x}, t) - u^2(\mathbf{x}, t)$  with  $h(\mathbf{x}, t)$  given. Here  $L$  represents an operator defined as follows:

$$L := \sum_{k=1}^m {}_0^C D_t^{\beta_k} - \Delta - \int \cdot d\mathbf{s}, \quad (1.2)$$

where the operator  $\int \cdot d\mathbf{s}$  denotes a Volterra or Fredholm integral,  ${}_0^C D_t^{\beta_k}$  denotes temporal Caputo fractional derivative of order  $\beta_k \in (0, 1) \cup (1, 2)$  for  $k = 1, 2, \dots, m$ , with  $\beta_1 < \beta_2 < \cdots < \beta_m$ . In practice, each term  ${}_0^C D_t^{\beta_k}$  could be multiplied by a positive constant, we set the constant to 1 here for simplicity. Multi-term fractional operators effectively capture multi-scale temporal behaviors and hierarchical system dynamics, offering enhanced modeling capabilities for processes exhibiting memory effects and heterogeneous relaxation times. For instance, Srivastava et al. [28] employ multi-term fractional diffusion equations to characterize oxygen subdiffusion in anisotropic media, while Torvik and Bagley [31] use two-term formulations to discriminate between solute transport regimes. A critical challenge in solving (1.1) arises from their inherent non-smoothness in the temporal direction, particularly exhibiting initial layer behaviors near  $t = 0$  [11, 27, 39]. To solve this difficulty, researchers have developed specialized numerical schemes. For example, She et al. [27] introduce a change of variable in the temporal direction and use a modified L1 approximation for the Caputo derivatives, combined with a Galerkin-spectral method for spatial discretization. Zeng et al. [38] design a modified formula with the appropriate correction terms.

Machine learning approaches solving (1.1) typically employ neural networks as trial functions and the residual of the equation as the loss function. They mainly focus on two aspects: calculation of the loss function, and optimization of neural network parameters. The nonlocal property makes TFPIDEs be high-dimensional integro-differential equations, posing fundamental challenges for efficiently computing the loss function. Among those ingredients, the most crucial one is to effectively approximate the Caputo derivative as well as the Fredholm or Volterra integral. Based on this consideration, this paper aims to design efficient numerical methods for solving TFPIDEs by combining time-space decoupled TNN with Gauss-Jacobi quadrature. Specifically, we propose a temporal-spatial separated TNN architecture where the TNN function is explicitly multiplied by  $t^\mu$ , where the power  $\mu$  defined in Subsection (2.2). This critical design achieves two advantages:

- When using spatiotemporal-separated TNNs as the trial function, the fractional derivative in the temporal direction can be straightforwardly generated by applying the fractional-order operator to the time-direction neural network in conjunction with spatial data, enabling parallel computation of the temporal and spatial derivatives. Additionally, the variable-separated structure of TNN enables the use of sufficient numerical integration points in the loss function calculation. Therefore, both the efficiency and accuracy of loss function computation are guaranteed.

- The TNN function with  $t^\mu$  inherently satisfies the homogeneous initial condition. Through numerical examples, we present a reasonable way to select the parameter  $\mu$ , which is related to the order of the fractional-order operator. This design is beneficial for neural network to approximate weak singular solutions and ensures the effectiveness of the Gauss-Jacobi quadrature.

Compared with fPINN methods and other machine learning methods, the method proposed in this paper shows obvious accuracy improvements for solving TFPIDEs (1.1).

An outline of the paper goes as follows. We introduce in Section 2 the TNN structure, the construction of the loss function, and the numerical schemes of Caputo derivatives, the Fredholm and Volterra integrals. In Section 3, the optimal TNN parameters are designed for solving linear and nonlinear TFPIDEs. Section 4 provides some numerical examples to validate the accuracy and efficiency of the proposed method.

## 2 Construction and computation of the loss function for solving TFPIDEs

In order to construct and compute the loss function based on TNN for solving TFPIDEs, in this section, we introduce the TNN structure containing time, the construction of the loss function, and the discrete process of the Caputo fractional derivative, the Fredholm integral and the Volterra integral.

### 2.1 Tensor neural network architecture

In this section, we introduce the TNN structure and its approximation properties and some techniques to improve the numerical stability. The approximation property and computational complexity of related integration associated with the TNN structure have been discussed in [34].

The TNN is built with  $d$  subnetworks, and each subnetwork is a continuous mapping from a bounded closed set  $\Omega_i \subset \mathbb{R}$  to  $\mathbb{R}^p$ , which can be expressed as

$$\Phi_i(x_i; \theta_i) = (\phi_{i,1}(x_i; \theta_i), \phi_{i,2}(x_i; \theta_i), \dots, \phi_{i,p}(x_i; \theta_i))^\top, \quad (2.1)$$

$$\Phi_t(t; \theta_t) = (\phi_{t,1}(t; \theta_t), \phi_{t,2}(t; \theta_t), \dots, \phi_{t,p}(t; \theta_t))^\top, \quad (2.2)$$

where  $i = 1, \dots, d$ , each  $x_i$  denotes the one-dimensional input,  $\theta_i$  denotes the parameters of the  $i$ -th subnetwork, typically the weights and biases. As illustrated in Figure 1, the TNN structure containing time is composed of  $p$  Feedforward Neural Networks (FNNs) for spatial basis functions  $\Phi_i(x_i; \theta_i)$ ,  $i = 1, 2, \dots, d$ , and one FNN for the temporal basis function  $\Phi_t(t; \theta_t)$ .

In order to improve the numerical stability, we normalize each  $\phi_{i,j}(x_i)$ ,  $\phi_{t,j}(t)$  and use the following normalized TNN structure:

$$\begin{aligned} \Psi(\mathbf{x}, t; c, \theta) &= \sum_{j=1}^p c_j \hat{\phi}_{1,j}(x_1; \theta_1) \cdots \hat{\phi}_{d,j}(x_d; \theta_d) \hat{\phi}_{t,j}(t; \theta_t) \\ &= \sum_{j=1}^p c_j \prod_{i=1}^d \hat{\phi}_{i,j}(x_i; \theta_i) \hat{\phi}_{t,j}(t; \theta_t) =: \sum_{j=1}^p c_j \varphi_j(\mathbf{x}, t; \theta), \end{aligned}$$

where each  $c_j$  is a scaling parameter with respect to the normalized rank-one function,  $c = \{c_j\}_{j=1}^p$  denotes the linear coefficients for the basis system built by the rank-one functions

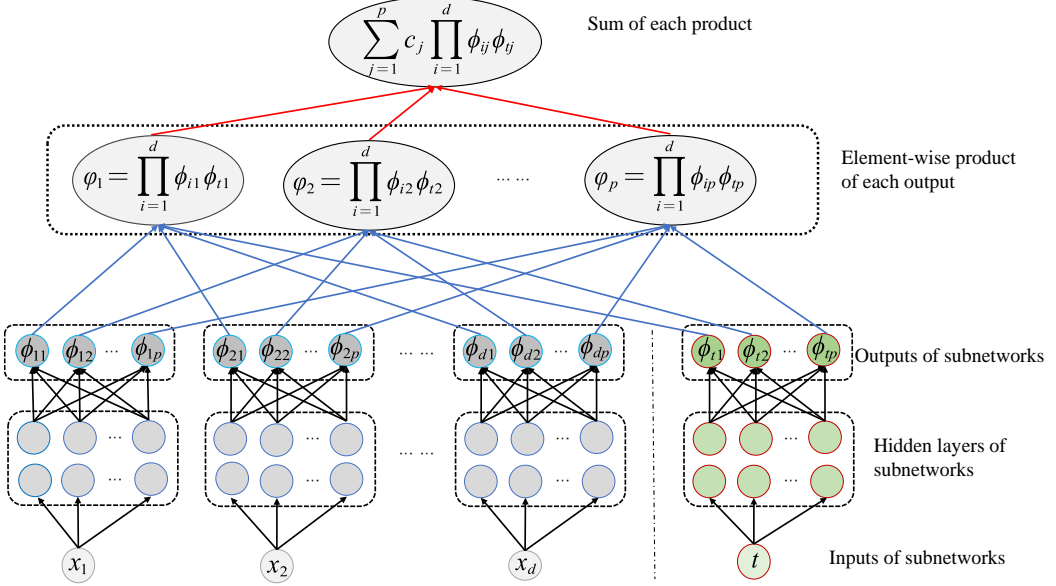


**Figure 1:** Architecture of spatiotemporal-separated TNN. Black arrows mean linear transformation (or affine transformation). Each ending node of blue arrows is obtained by taking the scalar multiplication of all starting nodes of blue arrows that end in this ending node. The final output of TNN is derived from the summation of all starting nodes of red arrows.

$\varphi_j(x, t; \theta)$ ,  $j = 1, \dots, p$ . For  $i = 1, \dots, d$ ,  $j = 1, \dots, p$ ,  $\hat{\phi}_{i,j}(x_i; \theta_i)$  and  $\hat{\phi}_{t,j}(t; \theta_t)$  are  $L^2$ -normalized function as follows:

$$\hat{\phi}_{i,j}(x_i; \theta_i) = \frac{\phi_{i,j}(x_i; \theta_i)}{\|\phi_{i,j}(x_i; \theta_i)\|_{L^2(\Omega_i)}}, \quad \hat{\phi}_{t,j}(t; \theta_t) = \frac{\phi_{t,j}(t; \theta_t)}{\|\phi_{t,j}(t; \theta_t)\|_{L^2(\Omega_t)}}. \quad (2.3)$$

For simplicity of notation,  $\phi_{i,j}(x_i; \theta_i)$  and  $\phi_{t,j}(t; \theta_t)$  denote the normalized function in the following parts.

Due to the isomorphism relation between  $L^2(\Omega_1 \times \dots \times \Omega_{d+1})$  and the tensor product space  $L^2(\Omega_1) \otimes \dots \otimes L^2(\Omega_{d+1})$  with  $\Omega_{d+1} := (0, T]$ , the process of approximating the function  $f(x, t) \in L^2(\Omega_1 \times \dots \times \Omega_{d+1})$  with the TNN defined by (2.3) is actually to search for a correlated CP decomposition to approximate  $f(x, t)$  in the space  $L^2(\Omega_1) \otimes \dots \otimes L^2(\Omega_{d+1})$  with rank not greater than  $p$ . Due to the low-rank structure, we will find that the polynomial mapping acting on the TNN and its derivatives can be done with small scale computational work [34]. In order to show the validity of solving PDEs by the TNN, we introduce the following approximation result to the functions of the space  $L^2(\Omega_1 \times \dots \times \Omega_{d+1})$  in the sense of  $H^m(\Omega_1 \times \dots \times \Omega_{d+1})$ -norm.

**Theorem 2.1.** [34] *Assume that each  $\Omega_i$  is a bounded closed interval in  $\mathbb{R}$  for  $i = 1, \dots, d$ ,  $\Omega = \Omega_1 \times \dots \times \Omega_d$ , and the function  $f(\mathbf{x}, t) \in H^m(\Omega \times (0, T])$ . Then for any tolerance  $\varepsilon > 0$ , there exists a positive integer  $p$  and the corresponding TNN basis functions defined by (2.3) such that the following approximation property holds*

$$\|f(\mathbf{x}, t) - \Psi(\mathbf{x}, t; c, \theta)\|_{H^m(\Omega \times [0, T])} < \varepsilon. \quad (2.4)$$

**Remark 2.1.** Note that for the spatial direction, we employ the variable-separated neural network, namely the TNN as well. While the non-variable-separated FNN can also be used, the advantage of using TNN is that the partial derivatives in the spatial direction can be efficiently

obtained, and the high-dimensional integration in the loss function can be transformed into a one-dimensional integration in some cases. Therefore, both the efficiency and accuracy in the calculation process of the loss function can be guaranteed. Meanwhile, the approximation ability of TNN makes it reasonable as a trial function to solve partial differential equations. In our numerical examples, we also present a problem whose exact solution is not in a variable-separated form, yet the TNN method still achieves high accuracy.

## 2.2 Construction of the loss function

Many studies have shown that an imbalance between PDE loss and initial/boundary loss may lead to a decrease in accuracy and significantly increase the training cost. Weighting techniques have been used to correct this imbalance [37, 40]. For this reason, in this section, we provide a method so that there is no need to introduce the penalty term to enforce the initial/boundary value conditions into the loss function. This can improve the convergence rate and stability of the training process.

If  $g(\mathbf{x}, t) = 0$  and  $s(\mathbf{x}) = 0$  in the problem (1.1), to ensure that the TNN function  $\Psi$  satisfies the boundary conditions, the formula for the left-hand side of (2.3) can be modified as follows:

$$\hat{\phi}_{i,j}(x_i; \theta_i) = \frac{\phi_{i,j}(x_i; \theta_i)(x_i - a_i)(b_i - x_i)}{\|\phi_{i,j}(x_i; \theta_i)(x_i - a_i)(b_i - x_i)\|_{L^2(\Omega_i)}}, \quad (2.5)$$

where the factor function  $(x_i - a_i)(b_i - x_i)$  is used for treating the homogeneous Dirichlet boundary conditions defined on  $\partial\Omega$ . In addition, we multiply the TNN function  $\Psi$  by the function  $b(t) = t^\mu$  with  $\mu > 0$ . The value of  $\mu$  has a great influence on the numerical results of TFPIDEs. For different cases of TFPIDEs (1.1), we adopt distinct strategies to select  $\mu$  in Section 4.1. Specifically,  $\mu = \beta$  for single-term TFPIDEs, whereas for multi-term TFPIDEs,  $\mu$  is explicitly defined as follows:

$$\mu = \begin{cases} \min_{i=1,2,\dots,m} \{\beta_i\}, & \text{if } \max_{i=1,2,\dots,m} \{\beta_i\} < 1, \\ \min_{i=1,2,\dots,m} \{\beta_i, \beta_i > 1\}, & \text{if } \max_{i=1,2,\dots,m} \{\beta_i\} > 1. \end{cases}$$

then gain the TNN function  $\Psi(\mathbf{x}, t; c, \theta)$  as follows:

$$\Psi(\mathbf{x}, t; c, \theta) = \sum_{j=1}^p c_j \prod_{i=1}^d \phi_{i,j}(x_i; \theta_i) t^\mu \phi_{t,j}(t; \theta_t).$$

On one hand, this treatment is necessary to insure that  $\Psi$  satisfies the initial condition; on the other hand, multiplying by  $t^\mu$  is critical for two key reasons:

- (a) For fractional orders  $\max_{i=1,2,\dots,m} \{\beta_i\} < 1$ : It significantly improves the approximation of weakly singular solutions by removing additional singularity of the TNN function caused by discretizing the Caputo fractional derivative.
- (b) For fractional orders  $\max_{i=1,2,\dots,m} \{\beta_i\} > 1$ : It is essential for ensuring the effectiveness of Gauss-Jacobi quadrature. If  $t^\mu$  is replaced by  $t$ , the Gauss-Jacobi numerical integration formula loses a key term, leading to a great degradation in accuracy.

Thus, the corresponding loss function is given by

$$\mathcal{L} = \|L\Psi(\mathbf{x}, t; c, \theta) - f(\mathbf{x}, t, \Psi(\mathbf{x}, t; c, \theta))\|_{\Omega \times (0, T]}. \quad (2.6)$$

For the non-homogeneous initial boundary value conditions, we introduce a new function  $\hat{g}(x, t) \in H^1(\Omega \times (0, T])$  such that

$$\hat{g}(\mathbf{x}, t) = g(\mathbf{x}, t), \quad (\mathbf{x}, t) \in \partial\Omega \times (0, T].$$

Then using the formula,

$$u(\mathbf{x}, t) = \hat{u}(\mathbf{x}, t) + s(\mathbf{x}) - g(\mathbf{x}, 0) + \hat{g}(\mathbf{x}, t), \quad (2.7)$$

the non-homogeneous initial boundary value problem is transformed into the corresponding homogeneous one. For more information about the treatment for nonhomogeneous boundary value conditions, please refer to [35].

### 2.3 Compute the Caputo fractional derivative

In this subsection, we use the Gauss-Jacobi quadrature scheme to compute the Caputo fractional derivative. The Caputo fractional derivative [9] of order  $\alpha > 0$  for the given function  $f(t)$ ,  $t \in (a, b)$  is defined as follows:

$${}_a^C D_t^\alpha f(t) = \frac{1}{\Gamma(n-\alpha)} \int_a^t (t-s)^{n-\alpha-1} f^{(n)}(s) ds, \quad (2.8)$$

where  $\Gamma(\cdot)$  denotes the Gamma function and  $n$  is a positive integer satisfying  $n-1 < \alpha \leq n$ .

The Gauss-Jacobi numerical integration is an efficient method for calculating definite integrals with high accuracy, it uses  $n$  nodes  $\{x_i\}_{i=1}^n$  and weights  $\{w_i\}_{i=1}^n$  to approximate the integral over  $[-1, 1]$  with a weighting function of  $(1-x)^\alpha(1+x)^\beta$  (cf. [2])

$$\int_{-1}^1 (1-x)^\alpha(1+x)^\beta f(x) dx = \sum_{i=1}^n w_i^{(\alpha, \beta)} f(x_i^{(\alpha, \beta)}) + R_n(f), \quad (2.9)$$

where  $\alpha > -1$ ,  $\beta > -1$ , the  $n$  nodes  $\{x_i^{(\alpha, \beta)}\}_{i=1}^n$  are the zeros of the Jacobi polynomial of degree  $n$ ,  $P_n^{(\alpha, \beta)}(x)$ . And the  $n$  weights  $\{w_i^{(\alpha, \beta)}\}_{i=1}^n$  can be calculated by the following formula,

$$w_i^{(\alpha, \beta)} = 2^{\alpha+\beta+1} \frac{\Gamma(\alpha+n+1)\Gamma(\beta+n+1)}{n!\Gamma(\alpha+\beta+n+1) \left(1 - \left(x_i^{(\alpha, \beta)}\right)^2\right) \left[P_n^{(\alpha, \beta)'}\left(x_i^{(\alpha, \beta)}\right)\right]^2}.$$

About the integration error  $R_n(f)$  and more information, please refer to [8].

We design the Gauss-Jacobi quadrature scheme on the interval  $[0, 1]$  as follows,

$$\int_0^1 (1-t)^\alpha t^\beta f(t) dt \approx \sum_{i=1}^n w_i^{(\alpha, \beta)} f(t_i^{(\alpha, \beta)}), \quad (2.10)$$

where  $t_i^{(\alpha, \beta)} = \frac{1}{2}\hat{t}_i^{(\alpha, \beta)} + \frac{1}{2}$  and  $w_i^{(\alpha, \beta)} = \frac{1}{2^{\alpha+\beta+1}}\hat{w}_i^{(\alpha, \beta)}$ ,  $\{\hat{t}_i^{(\alpha, \beta)}\}_{i=1}^n$ ,  $\{\hat{w}_i^{(\alpha, \beta)}\}_{i=1}^n$  are the nodes and weights of the Gauss-Jacobi quadrature on  $[-1, 1]$ .

For simplicity of notation,  $\phi_{i,j}(\cdot)$  and  $\phi_{t,j}(\cdot)$  denote  $\phi_{i,j}(\cdot, \theta_i)$  and  $\phi_{t,j}(\cdot, \theta_t)$ , respectively. Thus, for the left  $\nu$  order Caputo fractional derivative, when  $\nu \in (0, 1)$ , the interval  $[0, x]$  is transformed into  $[0, 1]$  by  $s = t\tau$  and using the formula (2.10), we have the following computing scheme,

$${}_0^C D_t^\nu t^\mu \phi_{t,j}(t)$$

$$\begin{aligned}
&= \frac{1}{\Gamma(1-\nu)} \int_0^1 (1-\tau)^{-\nu} [\mu(t\tau)^{\mu-1} \phi_{t,j}(t\tau) + (t\tau)^\mu \phi'_{t,j}(t\tau)] t^{1-\nu} d\tau \\
&\approx \frac{\mu t^{\mu-\nu}}{\Gamma(1-\nu)} \sum_{k=1}^{N_\tau} w_k^{(-\nu, \mu-1)} \phi_{t,j}(t\tau_k^{(-\nu, \mu-1)}) + \frac{t^{1+\mu-\nu}}{\Gamma(1-\nu)} \sum_{k=1}^{N_\tau} w_k^{(-\nu, \mu-1)} \tau_k^{(-\nu, \mu-1)} \phi'_{t,j}(t\tau_k^{(-\nu, \mu-1)}).
\end{aligned}$$

Similarly, when the fractional order  $\nu \in (1, 2)$ , we have the following computing scheme,

$$\begin{aligned}
&_0^C D_t^\nu t^\mu \phi_{t,j}(t) \\
&= \frac{1}{\Gamma(2-\nu)} t^{2-\nu} \int_0^1 (1-\tau)^{1-\nu} \tau^{\mu-2} [\mu(\mu-1)t^{\mu-2} \phi_{t,j}(t\tau) + 2\mu t^{\mu-1} \tau \phi'_{t,j}(t\tau) + t^\mu \tau^2 \phi''_{t,j}(t\tau)] d\tau \\
&\approx \frac{\mu(\mu-1)t^{\mu-\nu}}{\Gamma(2-\nu)} \sum_{k=1}^{N_\tau} w_k^{(1-\nu, \mu-2)} \phi_{t,j}(t\tau_k^{(1-\nu, \mu-2)}) \\
&\quad + \frac{2\mu t^{\mu-\nu+1}}{\Gamma(2-\nu)} \sum_{k=1}^{N_\tau} w_k^{(1-\nu, \mu-2)} \tau_k^{(1-\nu, \mu-2)} \phi'_{t,j}(t\tau_k^{(1-\nu, \mu-2)}) \\
&\quad + \frac{t^{2-\nu+\mu}}{\Gamma(2-\nu)} \sum_{k=1}^{N_\tau} w_k^{(1-\nu, \mu-2)} (\tau_k^{(1-\nu, \mu-2)})^2 \phi''_{t,j}(t\tau_k^{(1-\nu, \mu-2)}).
\end{aligned}$$

Using the fractional derivative operator  $_0^C D_t^\nu$  to the TNN function (2.3) leads to

$$_0^C D_t^\nu \Psi(\mathbf{x}, t; c, \theta) = \sum_{j=1}^p c_j \prod_{i=1}^d \phi_{i,j}(x_i; \theta_i) {}_0^C D_t^\nu t^\mu \phi_{t,j}(t; \theta_t).$$

Additionally, the Gauss-Jacobi quadrature is appropriate for evaluating Fredholm integrals with weakly singular kernels (see Subsection 4.2.2).

### 3 Machine learning method for TFPIDEs

This section is devoted to introducing a type of adaptive optimization of TNN parameters for solving TFPIDEs with high accuracy. The basic idea is to generate a subspace using the output functions of TNN as the basis functions, where we find an approximate solution in some sense. Then the training steps are adopted to update the TNN subspace to improve its approximation property.

We define the TNN subspace as follows:

$$V_p := \text{span} \left\{ \varphi_j(\mathbf{x}, t; \theta), j = 1, \dots, p \right\}, \quad (3.1)$$

where  $\varphi_j(\mathbf{x}, t; \theta)$  is the rank-one function defined in (2.3).

Then the subspace approximation procedure can be adopted to get the solution  $u_p \in V_p$ . For this purpose, in this paper, the subspace approximation  $u_p \in V_p$  for (1.1) is obtained by minimizing the residual  $Lu_p - f$  in the sense of  $L^2(\Omega \times (0, T])$ . Then the corresponding discrete problem can be given as: Find  $u_p \in V_p$  such that

$$(Lu_p, Lv_p) = (f, Lv_p), \quad \forall v_p \in V_p. \quad (3.2)$$

After obtaining the approximation  $u_p$ , the subspace  $V_p$  is updated by optimizing the loss function.

### 3.1 Solving linear TFPIDEs

In this subsection, we introduce the adaptive TNN subspace method to solve linear TFPIDEs. After the  $\ell$ -th training step, the TNN  $\Psi(\mathbf{x}, t; c, \theta^{(\ell)})$  belongs to the following subspace:

$$V_p^{(\ell)} := \text{span} \left\{ \varphi_j(\mathbf{x}, t; \theta^{(\ell)}), j = 1, \dots, p \right\},$$

where  $\varphi_j(\mathbf{x}, t; \theta^{(\ell)})$  is the rank-one function defined in (2.3) after  $\ell$  training steps.

According to the definition of TNN and the corresponding space  $V_p^{(\ell)}$ , it is easy to know that the neural network parameters  $\theta^{(\ell)}$  determine the space  $V_p^{(\ell)}$ , while the coefficient parameters  $c^{(\ell)}$  determine the direction of TNN in the space  $V_p^{(\ell)}$ . We can divide the optimization step into two sub-steps. Firstly, assume the neural network parameters  $\theta^{(\ell)}$  are fixed. The optimal coefficient parameters  $c^{(\ell+1)}$  can be obtained with the least squares method (3.2), i.e., by solving the following linear equation

$$A^{(\ell)} c^{(\ell+1)} = B^{(\ell)}, \quad (3.3)$$

where the matrix  $A^{(\ell)} \in \mathbb{R}^{p \times p}$  and the vector  $B^{(\ell)} \in \mathbb{R}^{p \times 1}$  are assembled as follows:

$$A_{m,n}^{(\ell)} = (L\varphi_n^{(\ell)}, L\varphi_m^{(\ell)}), \quad B_m^{(\ell)} = (f, L\varphi_m^{(\ell)}), \quad 1 \leq m, n \leq p.$$

**Remark 3.1.** *In the process of solving equation (3.3) to obtain the coefficients  $c^{(\ell+1)}$ , the equation may become ill-conditioned due to the linear dependence of the basis functions  $\varphi_j(\mathbf{x}, t; \theta)$ ,  $j = 1, \dots, p$ . In such cases, we can employ techniques such as singular value decomposition (SVD) or other methods to obtain the coefficients  $c^{(\ell+1)}$ . In this article, we solve this problem by solving the linear system (3.3) using ridge regression as follows:*

$$\left( (A^{(\ell)})^\top A^{(\ell)} + \lambda E \right) c^{(\ell+1)} = (A^{(\ell)})^\top B^{(\ell)}, \quad (3.4)$$

where  $\lambda$  is the regularization parameter, which is chosen empirically as  $1 \times 10^{-5}$  and  $E$  is the identity matrix.

Secondly, when the coefficient parameters  $c^{(\ell+1)}$  are fixed, the neural network parameters  $\theta^{(\ell+1)}$  can be updated by the optimization steps included, such as Adam or L-BFGS for the loss function  $\mathcal{L}^{(\ell+1)}(c^{(\ell+1)}, \theta^{(\ell)})$  defined in Subsection 2.2. Thus, the TNN-based machine learning method for the homogeneous Dirichlet boundary and initial value problem can be defined in Algorithm 1. This type of parameter optimization significantly enhances the efficiency of the training process and effectively improves the accuracy of the TNN method.

### 3.2 Solving nonlinear TFPIDEs

This subsection is devoted to designing a TNN-based machine learning method for solving nonlinear problems (1.1). Here, the operator of the problem (1.1) with respect to the unknown solution  $u$  is assumed to be expressed as  $L_1 + G$ , where  $L_1$  is a linear operator and  $G$  is a nonlinear operator. Specifically, in this paper, we consider the following two cases:

$$G(u)(\mathbf{x}, t) = u^2(\mathbf{x}, t), \quad (3.5)$$

$$G(u)(t) = \int k(\mathbf{s}, t) u^2(\mathbf{s}, t) d\mathbf{s}. \quad (3.6)$$

We denote the solution at the  $k$ -th outer iteration and  $\ell$ -th inner iteration as  $u^{(k,\ell)}$

$$u^{(k,\ell)} = \Psi(\mathbf{x}, t; c^{(\ell)}, \theta^{(k)}).$$

---

**Algorithm 1:** Adaptive TNN subspace method for linear TFPIDEs

---

1. Initialization: Build the initial TNN  $\Psi(\mathbf{x}, t; c^{(0)}, \theta^{(0)})$  defined in Subsection 2.2, set the loss function  $\mathcal{L}(\Psi(\mathbf{x}, t; c, \theta))$ , the maximum number of training steps  $M$ , learning rate  $\gamma$ , and the iteration counter  $\ell = 0$ .
2. Define the subspace  $V_p^{(\ell)}$  as follows:

$$V_p^{(\ell)} := \text{span} \left\{ \varphi_j(\mathbf{x}, t; \theta^{(\ell)}), j = 1, \dots, p \right\}.$$

Assemble the stiffness matrix  $A^{(\ell)} \in \mathbb{R}^{p \times p}$  and right-hand side term  $B^{(\ell)} \in \mathbb{R}^p$  on  $V_p^{(\ell)}$ :

$$A_{m,n}^{(\ell)} = (L\varphi_n^{(\ell)}, L\varphi_m^{(\ell)}), \quad B_m^{(\ell)} = (f, L\varphi_m^{(\ell)}) \quad 1 \leq m, n \leq p,$$

where  $L(\cdot)$  is calculated in Subsection 2.3.

3. Solve the following linear system to determine the coefficient vector  $c \in \mathbb{R}^p$

$$A^{(\ell)}c = B^{(\ell)}.$$

Update  $\Psi(\mathbf{x}, t; c^{(\ell+1)}, \theta^{(\ell)})$  with the coefficient vector:  $c^{(\ell+1)} = c$ .

4. Update the network parameters from  $\theta^{(\ell)}$  to  $\theta^{(\ell+1)}$ , by optimizing the loss function  $\mathcal{L}^{(\ell+1)}(c^{(\ell+1)}, \theta^{(\ell)})$  through gradient-based training steps.
5. Iteration: set  $\ell = \ell + 1$ . If  $\ell < M$ , go to Step 2. Otherwise, terminate.

---

The iterative method for solving nonlinear problem (1.1) consists of outer and inner iteration steps. In the outer iteration step, the coefficient  $c^{(\ell)}$  is fixed, and only the network parameters  $\theta^{(k)}$  are updated by the loss function. When the inner iteration is performed, the network parameters  $\theta^{(k)}$  are fixed, and the optimal coefficient parameters  $c^{(\ell+1)}$  can be obtained by using the fixed-point iteration. Of course, other types of nonlinear iteration methods can also be used here.

Firstly, we introduce the inner iteration process. Starting from the current solution  $u^{(k,\ell)}$ , the next step in the inner iteration involves solving the following linear equation:

$$L_1 u^{(k,\ell+1)} + \widehat{G}(u^{(k,\ell)}, u^{(k,\ell+1)}) = h, \quad (3.7)$$

where  $h$  is defined in (1.1) and  $\widehat{G}(u^{(k,\ell)}, u^{(k,\ell+1)})$  is defined as follows

$$\widehat{G}(u^{(k,\ell)}, u^{(k,\ell+1)}) = u^{(k,\ell)} u^{(k,\ell+1)}, \quad (3.8)$$

$$\widehat{G}(u^{(k,\ell)}, u^{(k,\ell+1)}) = \int k(\mathbf{s}, t) u^{(k,\ell)}(\mathbf{s}, t) u^{(k,\ell+1)}(\mathbf{s}, t) d\mathbf{s}. \quad (3.9)$$

In order to solve the linear system (3.7), we assemble the stiffness matrix  $A^{(\ell+1)}$  and the right-hand side term  $B^{(\ell+1)}$  as follows

$$\begin{aligned} A_{m,n}^{(\ell+1)} &= (F\varphi_m(\mathbf{x}, t; \theta^{(k)}), F\varphi_n(\mathbf{x}, t; \theta^{(k)})), \quad 1 \leq m, n \leq p, \\ B_m^{(\ell+1)} &= (F\varphi_m(\mathbf{x}, t; \theta^{(k)}), h), \quad 1 \leq m \leq p, \end{aligned}$$

where the term  $F\varphi_m(\mathbf{x}, t, \theta^{(k)})$  is defined as follows

$$F\varphi_m(\mathbf{x}, t; \theta^{(k)}) := L_1\varphi_m(\mathbf{x}, t; \theta^{(k)}) + \sum_{j=1}^p c_j^{(\ell)} \widehat{G}(\varphi_j(\mathbf{x}, t; \theta^{(k)}), \varphi_m(\mathbf{x}, t; \theta^{(k)})), \quad (3.10)$$

where  $\widehat{G}(\cdot, \cdot)$  is defined in (3.8) or (3.9). Then solve the linear system  $A^{(\ell+1)}c = B^{(\ell+1)}$  and update the new coefficient vector  $c^{(\ell+1)} = c$ .

After completing the inner iterations, we obtain the solution  $u^{(k, M_2)}$ . To initiate the outer iteration, we define a loss function as follows:

$$\mathcal{L}^{(k+1)}(c^{(M_2)}, \theta^{(k)}) := \left\| L_1 u^{(k, M_2)} - G(u^{(k, M_2)}) - h \right\|_{\Omega \times (0, T]}, \quad (3.11)$$

where  $G(\cdot)$  is defined in (3.5) or (3.6). For the detailed information about the construction of the loss function, please see Subsection 2.2. Then update the network parameters  $\theta^{(k)}$  to obtain  $\theta^{(k+1)}$  by the optimization steps included, such as Adam or L-BFGS for the loss function  $\mathcal{L}^{(k+1)}(c^{(M_2)}, \theta^{(k)})$ .

As evident from the above description, the overall solution process is almost the same as that for solving linear TFPIDEs, with the only difference lying in the way of obtaining the parameter  $c^{\ell+1}$ . For simplicity, we do not state the corresponding algorithm for solving nonlinear TFPIDEs.

## 4 Numerical examples

In this section, we provide several examples to validate the efficiency and accuracy of the proposed TNN-based machine learning method. All the experiments are done on an NVIDIA Tesla A800 GPU and an Tesla NVIDIA V100 GPU.

The following two notations about the approximate solution  $\Psi(\mathbf{x}, t; c, \theta)$  and the exact solution  $u$  are used to measure the convergence behavior and accuracy of the examples in this section:

- Relative  $L^2$  norm error

$$e_{L^2} := \frac{\|u - \Psi(\mathbf{x}, t; c, \theta)\|_{L^2(\Omega)}}{\|u\|_{L^2(\Omega)}},$$

Here  $\|\cdot\|_{L^2}$  denotes the  $L^2(\Omega)$  norm.

- Relative  $L^2$  error at the test points

$$e_{\text{test}} := \frac{\sqrt{\sum_{k=1}^K (\Psi(x^k, t^k; c, \theta) - u(x^k, t^k))^2}}{\sqrt{\sum_{k=1}^K (u(x^k, t^k))^2}},$$

where the selected test points  $\{(x^k, t^k)\}$  on  $\Omega \times (0, T]$  are defined on a uniform grid of 300 spatial points and 300 temporal points for one-dimensional FPDEs. For the three-dimensional case in Subsection 4.3.3, the test points are defined on a uniform grid of  $30^3$  spatial points and 30 temporal points.

For all examples, the number of Jacobi quadrature nodes is set to 100, each FNN has three hidden layers with 50 neurons and the Tanh as activation function in each layer, the rank parameter for the TNN is set to be  $p = 50$ , and set the TNN function such that it can automatically satisfy the initial/boundary value conditions to approximate  $\hat{u}(\mathbf{x}, t)$ .

For one-dimensional examples, during computing the loss function, the interval along the  $x$ - or  $t$ -axis is subdivided into 25 subintervals with 16 Gauss points selected within each subinterval for building the quadrature scheme. The TNN is optimized using the Adam optimizer with an initial learning rate of 0.003 and automatically adjusts the learning rate for the 5000 epochs.

**Remark 4.1.** *In practical applications, the source term may be provided as vector-valued data rather than an explicit formula. To address this, TNN interpolation can be used to approximate the source term in a tensor-product format, ensuring compatibility with the tensor-network structure of the solver, please see [15].*

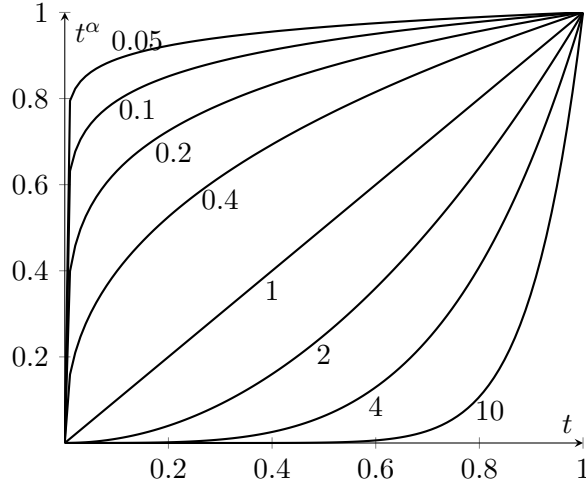


**Figure 2:** Function  $t^\alpha$  for various  $\alpha$  values

#### 4.1 Linear time-fractional diffusion-wave equations

We consider in this subsection the one-dimensional linear time-fractional diffusion wave equation with single-term or multi-term temporal Caputo derivatives: Find  $u(x, t)$  such that

$$\begin{cases} \sum_{k=1}^m {}_0^C D_t^{\beta_k} u(x, t) = \frac{\partial^2 u(x, t)}{\partial x^2} + f(x, t), & (x, t) \in \Omega \times (0, T], \\ u(x, t) = 0, & (x, t) \in \partial\Omega \times (0, T], \\ u(x, 0) = s(x), & x \in \Omega, \end{cases} \quad (4.1)$$

This is the simplest case of the general problem (1.1), the interested readers are referred to [6, 9, 10, 18, 25, 27, 28, 31, 39].

The performance of the proposed TNN-based machine learning method for solving (4.1) with the form  $t^\alpha$  ( $\alpha > 0$ ) as the exact solution is investigated. Figure 2 shows that  $t^\alpha$ ,  $\alpha \in (0, 1)$  has singularity at 0, which becomes more obvious as  $\alpha$  decreases from 1 to 0. In addition, when  $\alpha > 1$ , the function  $t^\alpha$  becomes smoother.

##### 4.1.1 Single-term time-fractional diffusion-wave equations

In this subsection, we consider the single-term time-fractional diffusion wave equation (4.1).

In the first example, we set the exact solution as  $u(x, t) = (t^{\alpha_2} + t^{\alpha_1}) \sin(2\pi x)$  with  $\alpha_1 \leq \alpha_2$ ,  $\alpha_1, \alpha_2 \in (0, 4)$ ,  $\beta < \alpha_1 + 0.5$ . For this aim, the initial value condition should be  $s(x) = 0$  and

the source term

$$f(x, t) = \left[ \sum_{i=1}^2 \frac{\Gamma(\alpha_i + 1) t^{\alpha_i - \beta}}{\Gamma(1 - \beta + \alpha_i)} + 4\pi^2(t^{\alpha_2} + t^{\alpha_1}) \right] \sin(2\pi x). \quad (4.2)$$

**Table 1:** Errors of the single-term time-fractional diffusion wave equation (4.1) for different values of  $\beta$  with  $\mu = \beta$  and different  $\alpha_1, \alpha_2 \in (0, 4)$ .

$\beta$	$(\alpha_1, \alpha_2)$	$e_{\text{test}}$	$\beta$	$(\alpha_1, \alpha_2)$	$e_{\text{test}}$
0.01	(0.01, 0.01)	6.395e-08	1.10	(1.20, 1.40)	5.405e-07
0.10	(0.15, 0.20)	1.352e-05	1.50	(1.60, 1.70)	6.635e-07
0.01	(0.20, 0.30)	1.537e-05	1.30	(1.20, 1.40)	3.001e-06
0.20	(0.80, 0.90)	6.017e-06	1.65	(1.60, 1.80)	5.130e-07
0.50	(0.01, 0.01)	2.067e-04	1.40	(2.00, 2.40)	1.707e-07
0.40	(0.15, 0.20)	7.618e-05	1.70	(2.10, 2.90)	7.389e-07
0.50	(1.40, 1.60)	7.350e-07	1.40	(3.00, 3.40)	7.412e-08
0.60	(2.30, 2.80)	4.362e-07	1.70	(3.50, 3.80)	2.307e-08

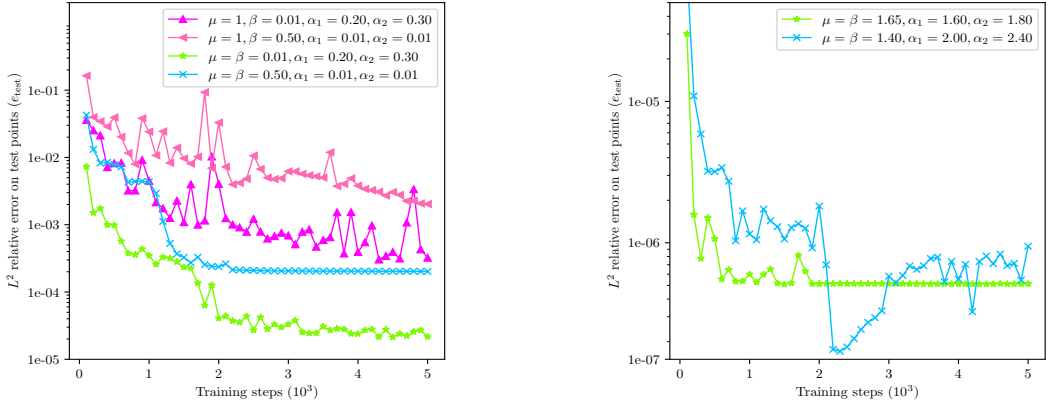


**Figure 3:** The loss curve and relative  $L^2$  error during the training process for solving the single-term time-fractional diffusion wave equation (4.1) with the exact solution  $u(x, t) = (t^{\alpha_1} + t^{\alpha_2}) \sin(2\pi x)$ .

The corresponding numerical results with  $\beta \in (0, 2)$  are shown in Table 1. From the table, it can be seen that the relative error attains around  $1 \times 10^{-5}$  for  $\beta \in (0, 1)$  when  $\alpha_1, \alpha_2 \in (0, 1)$  and  $\alpha_1, \alpha_2 > \beta$ . However, the relative error degrades slightly when  $\alpha_1$  or  $\alpha_2$  are less than  $\beta$ . The left side of Figure 3 shows that the relative error is significantly improved when choosing  $\mu = \beta$  rather than  $\mu = 1$ . The top and middle of Figure 4 show that the absolute error is relatively large at time close to  $t = 0$  when  $\alpha_1 = \alpha_2 = 0.01$  and  $\mu = \beta$ , it is the worst-case, but it still achieves a relative error of  $2.067 \times 10^{-4}$ . Notably, when  $\mu = \alpha_1 = \alpha_2 = 0.01$ , the relative error gets  $6.395 \times 10^{-8}$ . When  $\alpha_1, \alpha_2 \in (1, 3)$ , the function's smoothness improves, which leads to the relative error run up to  $1 \times 10^{-7}$ . Similarly, there is a slight decrease in relative error for  $\beta \in (1, 2)$  and  $\alpha_1, \alpha_2 < \beta$ . If  $\alpha_1, \alpha_2 \in (2, 3)$ , the function becomes smooth and the relative error gets about  $1 \times 10^{-7}$ . Furthermore, the relative error can arrive at about  $1 \times 10^{-8}$  when  $\alpha_1, \alpha_2 \in (3, 4)$ .

Additionally, when  $\beta \in (0, 1)$  and  $\beta > \alpha_1$ , the fPINN method fails to solve this problem, whereas the TNN method achieves a relative error of around  $1 \times 10^{-5}$ . When  $\beta \in (0, 1)$  and  $\beta < \alpha_1$ , the relative error of the fPINN method ranges between  $1 \times 10^{-2}$  and  $1 \times 10^{-3}$ ,

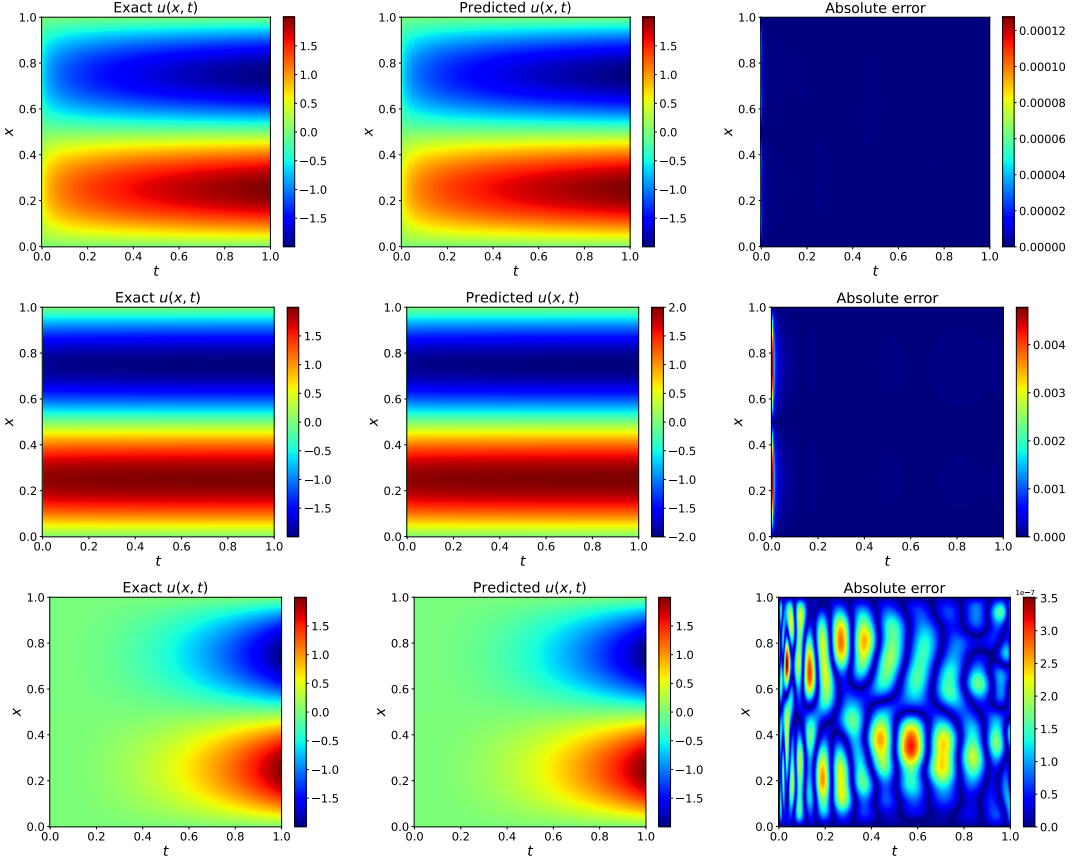


**Figure 4:** Numerical results of the single-term time-fractional diffusion wave equation (4.1) with  $u(x, t) = (t^{\alpha_1} + t^{\alpha_2}) \sin(2\pi x)$  for  $\alpha_1 = 0.20, \alpha_2 = 0.30$ , and  $\mu = \beta = 0.01$  (top row);  $\alpha_1 = 0.01, \alpha_2 = 0.01$ , and  $\mu = \beta = 0.5$  (middle row);  $\alpha_1 = 1.40, \alpha_2 = 2.0$ , and  $\mu = \beta = 2.4$  (bottom row): the exact solutions (left column), the predictions (middle column), and the absolute errors of approximation (right column).

with the error improving as the smoothness of the exact solution increases. Notably, when  $\beta = \alpha_1 = \alpha_2 = 0.01$ , the relative error of fPINN is only  $1 \times 10^{-1}$ . These results indicate that fPINN is relative difficult to solve this problem.

In the second example, we investigate the performance of the TNN-based machine learning method and compare it with other types of machine learning methods when the exact solution is a high-frequency function.

For  $\beta \in (0, 1)$ , the exact solution of (4.1) with  $m = 1$  is set to be  $u(x, t) = (t^\beta + 1) \sin(6\pi x)$  as in [25] with the initial value condition  $s(x) = \sin(6\pi x)$  and the source term

$$f(x, t) = \left[ \Gamma(\beta + 1) + 36\pi^2(t^\beta + 1) \right] \sin(6\pi x).$$

In addition, for  $1 < \beta < 2$ , we choose the exact solution to of (4.1) with  $m = 1$  as  $u(x, t) = (t^\beta + 1) \sin(4\pi x)$  for the initial value condition  $s(x) = \sin(4\pi x)$  and the source term

$$f(x, t) = [\Gamma(\beta + 1) + 16\pi^2(t^\beta + 1)] \sin(4\pi x).$$

Obviously, the solutions of this differential equation have relatively high oscillation. Let us do the decomposition  $u(x, t) = \hat{u}(x, t) + s(x)$  and build the TNN function to approximate  $\hat{u}(x, t)$  with the homogeneous initial value condition. The corresponding numerical results are shown

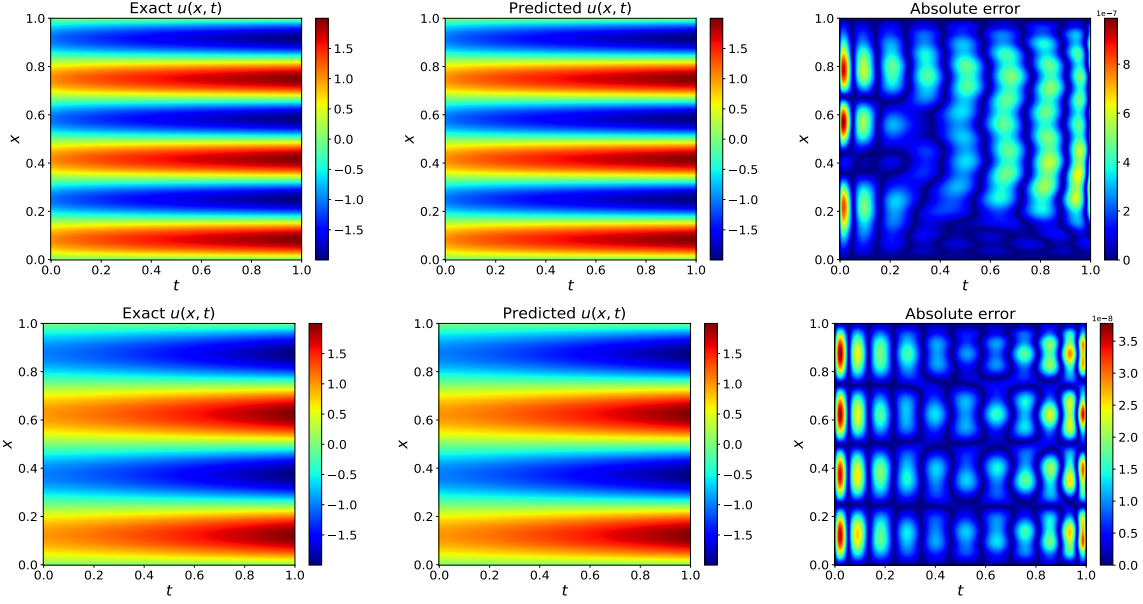


**Figure 5:** Numerical results of the single-term time-fractional diffusion wave equation (4.1) with exact solutions  $u(x, t) = (t^\beta + 1) \sin(6\pi x)$  for  $\mu = \beta = 0.70$  (top row) and  $u(x, t) = (t^\beta + 1) \sin(4\pi x)$  for  $\mu = \beta = 1.20$  (bottom row): the exact solutions (left column), the predictions (middle column) and the absolute errors of approximation (right column).

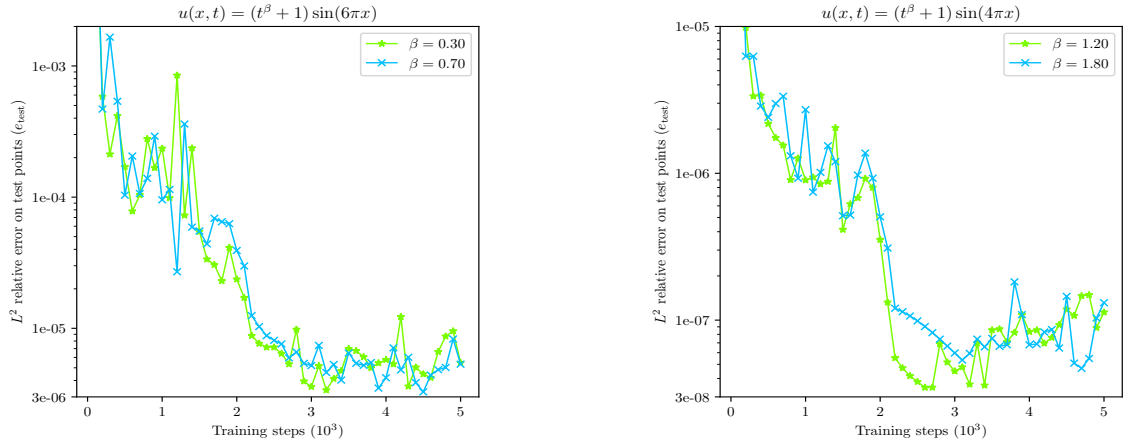


**Figure 6:** The relative  $L^2$  error during the training process for solving single-term time-fractional diffusion wave equation (4.1) with the exact solutions  $u(x, t) = (t^\beta + 1) \sin(6\pi x)$  (left) and  $u(x, t) = (t^\beta + 1) \sin(4\pi x)$  (right).

**Table 2:** Errors of the single-term time-fractional diffusion wave equation (4.1) for the exact solutions  $u(x, t) = (t^\beta + 1) \sin(6\pi x)$ ,  $\beta = 0.7$  and  $u(x, t) = (t^\beta + 1) \sin(4\pi x)$ ,  $\beta = 1.2$  by using fPINNs, IFPINNs and TNN ( $\mu = \beta$ ) methods.

$u(x, t) = (t^\beta + 1) \sin(6\pi x)$				$u(x, t) = (t^\beta + 1) \sin(4\pi x)$			
$\beta$	fPINNs [25]	IFPINNs [25]	TNNs	$\beta$	fPINNs [25]	IFPINNs [25]	TNNs
0.7	5.0e-01	2.9e-02	5.181e-06	1.2	6.6e-02	6.6e-02	5.882e-08

in Figures 5 and 6, Table 2, which show that the TNN method for the problem has an extremely high accuracy, while fPINNs or IFPINNs cannot solve this problem well (Table 2). This reflects

the high efficiency of the adaptive TNN subspace method proposed in this paper for the example here.

In summary, the accuracy of solving the single-term time fractional diffusion-wave equation increases with the smoothness of the exact solution. The reason should be that the neural networks are relatively easy to approximate continuous functions and not so easy to deal with the extra singularity of the solution when discretizing the Caputo fractional derivative by using the Gauss-Jacobi quadrature in Subsection 2.3. Furthermore, the exact solutions with  $t^\alpha$  have weak singularities for  $\alpha \in (0, 1)$ . Choosing  $\mu = \beta$  rather than  $\mu = 1$  for designing the TNN function to deal with the initial condition can improve accuracy. Meanwhile, choosing  $\mu = 1$  is not suitable for discrete Caputo fractional derivative in Subsection 2.3 when the exact solution becomes smooth for  $\beta \in (1, 2)$ . Therefore, for  $\beta \in (0, 2)$ , a relative good choice is  $\mu = \beta$ .

#### 4.1.2 Multi-term time-fractional diffusion-wave equations

Here, let us consider solving the following one-dimensional multi-term time fractional diffusion equations (4.1). For this aim, we choose the exact solution to (4.1) with  $m = 2$  as  $u(x, t) = (t^{\alpha_2} + t^{\alpha_1}) \sin(2\pi x)$ ,  $\alpha_1 \leq \alpha_2$ ,  $\alpha_1, \alpha_2 \in (0, 4)$ ,  $\beta_2 < \alpha_1 + 0.5$  by setting the initial value condition  $s(x) = 0$  and the source term

$$f(x, t) = \left[ \sum_{i=1}^2 \sum_{j=1}^2 \frac{\Gamma(1 + \alpha_j) t^{\alpha_j - \beta_i}}{\Gamma(1 + \alpha_j - \beta_i)} + 4\pi^2(t^{\alpha_2} + t^{\alpha_1}) \right] \sin(2\pi x). \quad (4.3)$$

The corresponding numerical results are shown in Table 3. From this table, it can be seen

**Table 3:** Errors of two-term time-fractional diffusion wave equation (4.1) for different values of  $\beta_1, \beta_2 \in (0, 1)$  or  $\beta_1, \beta_2 \in (1, 2)$  with  $\mu = \beta_1$  and different  $\alpha_1, \alpha_2 \in (0, 4)$ .

$(\beta_1, \beta_2)$	$(\alpha_1, \alpha_2)$	$e_{\text{test}}$	$(\beta_1, \beta_2)$	$(\alpha_1, \alpha_2)$	$e_{\text{test}}$
(0.20, 0.30)	(0.40, 0.80)	1.747e-05	(1.10, 1.65)	(1.20, 1.80)	5.009e-05
(0.10, 0.60)	(0.70, 0.90)	2.896e-06	(1.40, 1.50)	(1.20, 1.80)	3.509e-05
(0.20, 0.50)	(0.10, 1.00)	1.907e-05	(1.10, 1.70)	(2.20, 2.40)	5.314e-07
(0.60, 0.80)	(0.40, 0.80)	8.647e-05	(1.30, 1.90)	(2.20, 2.40)	9.042e-07
(0.50, 0.80)	(1.20, 1.40)	1.190e-06	(1.10, 1.50)	(3.50, 3.60)	1.193e-07
(0.10, 0.50)	(2.20, 2.40)	2.692e-07	(1.30, 1.80)	(3.50, 3.60)	2.686e-08

that the relative error attains around  $1 \times 10^{-5}$  for  $\beta_1, \beta_2 \in (0, 1)$  when  $\alpha_1, \alpha_2 \in (0, 1)$  or  $\beta_1, \beta_2 \in (1, 2)$  when  $\alpha_1, \alpha_2 \in (1, 2)$ . And the relative error will increase with the improvement of the smoothness of the exact solution for  $\beta_1, \beta_2 \in (0, 2)$ .

**Table 4:** Errors of four-term time-fractional diffusion wave equation (4.1) for different values of  $\beta_1, \beta_2 \in (0, 1), \beta_3, \beta_4 \in (1, 2)$  with  $\mu = \beta_3$  and different  $\alpha_1, \alpha_2 \in (0, 4)$ .

$\beta = (\beta_1, \beta_2, \beta_3, \beta_4)$	$(\alpha_1, \alpha_2)$	$e_{\text{test}}$
(0.20, 0.70, 1.10, 1.20)	(0.95, 1.90)	1.422e-05
(0.20, 0.30, 1.10, 1.45)	(1.30, 1.90)	9.082e-06
(0.30, 0.60, 1.30, 1.45)	(2.10, 2.50)	1.243e-07
(0.40, 0.90, 1.40, 1.85)	(3.20, 3.60)	9.587e-08

The next example is to consider solving (4.1) with  $m = 4$ . We set the initial value condition

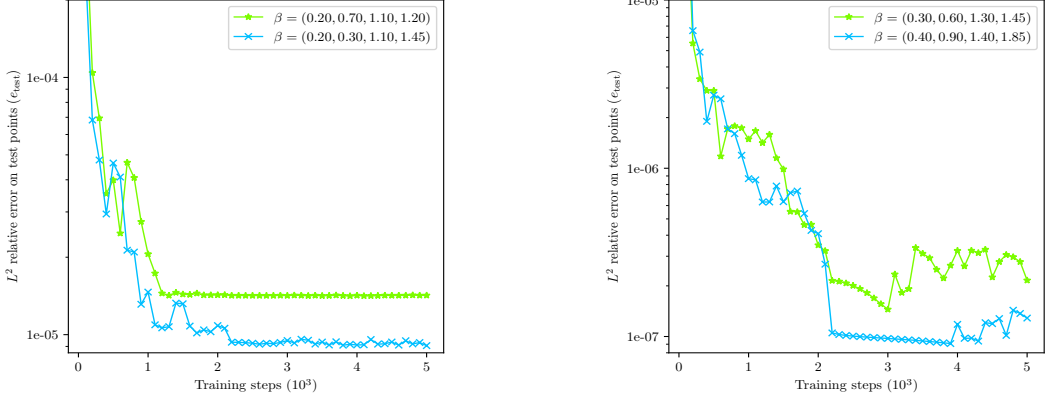


**Figure 7:** The relative  $L^2$  errors during the training process for solving four-term time-fractional diffusion wave equation (4.1).

$s(x) = 0$  and the source term

$$f(x, t) = \left[ \sum_{i=1}^4 \sum_{j=1}^2 \frac{\Gamma(1 + \alpha_j) t^{\alpha_j - \beta_i}}{\Gamma(1 + \alpha_j - \beta_i)} + 4\pi^2 (t^{\alpha_2} + t^{\alpha_1}) \right] \sin(2\pi x), \quad (4.4)$$

such that the exact solution is  $u(x, t) = (t^{\alpha_2} + t^{\alpha_1}) \sin(2\pi x)$  for  $\alpha_1 \leq \alpha_2$ ,  $\alpha_1, \alpha_2 \in (0, 1)$  and  $\beta_4 < \alpha_1 + 0.5$ .

If  $\beta_1, \beta_2 \in (0, 1)$ ,  $\beta_3, \beta_4 \in (1, 2)$ , the corresponding numerical results are shown in Table 4 and Figure 7, which show that the high efficiency of the TNN method is presented in this paper.

## 4.2 Nonlinear TFPIDEs with Fredholm integral

In this subsection, we focus on solving one-dimensional single/ multi-term nonlinear TFPIDEs (1.1) with Fredholm integral. Due to space constraints, this subsection presents two one-dimensional nonlinear examples, higher-dimensional cases are discussed in a Subsection (4.3).

### 4.2.1 Single-term time-fractional Fredholm IDE

Here, let us consider the following single-term TFPIDE, which includes a nonlinearity embedded within the Fredholm integral. This setup is designed to validate the capability of our method in solving TFPIDEs involving nonlinear integral terms.: Find  $u(x, t)$  such that

$$\begin{cases} {}_0^C D_t^\beta u(x, t) = \frac{\partial^2 u(x, t)}{\partial x^2} + f(x, t) \\ \quad + \frac{1}{2} \cos(x) \int_{-\frac{\pi}{2}}^{\frac{\pi}{2}} s t u^2(s, t) ds, \quad (x, t) \in [-\pi/2, \pi/2] \times (0, 1], \\ u(x, 0) = 0, \quad x \in [-\pi/2, \pi/2], \\ u(-\pi/2, t) = u(\pi/2, t) = 0, \quad t \in (0, 1], \end{cases} \quad (4.5)$$

where  $\beta \in (0, 1)$ .

For the first example, the exact solution is  $u(x, t) = (t^\beta + t) \cos(x)$  by choosing the source term

$$f(x, t) = \left[ \Gamma(1 + \beta) + 1/\Gamma(2 - \beta) t^{1-\beta} + (t^\beta + t) \right] \cos(x).$$

The exact solution for the second example is  $u(x, t) = t^\beta \cos(x)$  [40] by setting the source term as

$$f(x, t) = \Gamma(1 + \beta) \cos(x) + t^\beta \cos(x).$$

The following formula is the numerical scheme for the Fredholm integral in (4.5)

$$\int_{-\frac{\pi}{2}}^{\frac{\pi}{2}} \cos(x) t s \Psi^2(s, t) ds \approx \sum_{i=1}^p \sum_{j=1}^p c_i c_j \cos(x) \sum_{k=1}^{N_s} w_k s_k \phi_{1,i}(s_k) \phi_{1,j}(s_k) t^{2\mu+1} \phi_{t,i}(t) \phi_{t,j}(t),$$

where  $\{w_k, s_k\}_{k=1}^{N_m}$  are the nodes and weights of Gauss-Legendre quadrature in interval  $[-\pi/2, \pi/2]$ . This interval is subdivided into 25 subintervals, with 16 Gauss points selected within each subinterval to ensure sufficient accuracy for discretizing this Fredholm integral.

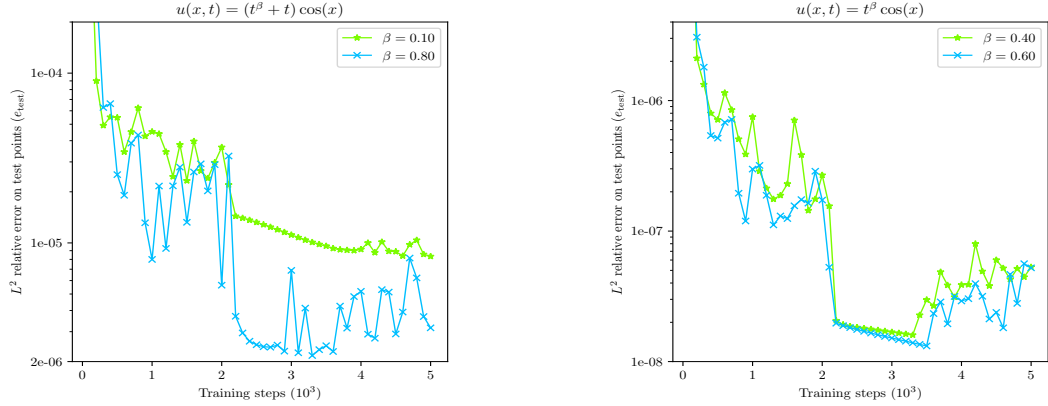


**Figure 8:** The relative  $L^2$  error during the training process for solving equation (4.5) with exact solutions  $u(x, t) = (t^\beta + t) \cos(x)$  (left) and  $u(x, t) = t^\beta \cos(x)$  (right).

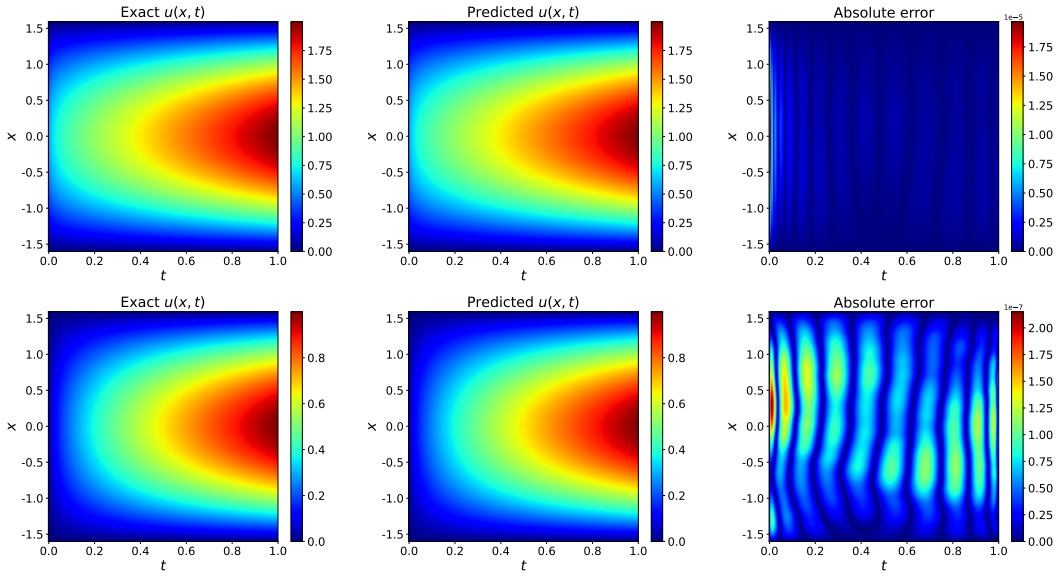


**Figure 9:** Numerical results of simple-term nonlinear TFPIDE with Fredholm integrals for the exact solutions  $u(x, t) = (t^\beta + t) \cos(x)$ ,  $\beta = 0.10$  (top row) and  $u(x, t) = t^\beta \cos(x)$ ,  $\beta = 0.60$  (bottom row): the exact solutions (left column), the predictions (middle column), and the absolute errors (right column) with  $\mu = \beta$ .

The corresponding numerical results are shown in Figures 8 and 9, and Table 5. Figures 8 and 9 show the relative  $L^2$  error during the training process and curves of the numerical results for the TNN method. Table 5 shows that the relative error can reach  $1 \times 10^{-8}$  for the case of the exact solution  $u(x, t) = t^\beta \cos(x)$ . The numerical comparison is included in Table 6, which

**Table 5:** Errors of single-term time fractional Fredholm IDE with  $\mu = \beta$ .

$\beta$	$e_{L^2}$	$e_{\text{test}}$
0.1	1.135e-05	8.688e-06
0.8	3.408e-06	3.348e-06

shows that AO-fPINNs and AWAO-fPINNs can only obtain the accuracy of  $1 \times 10^{-3}$  or  $1 \times 10^{-4}$ , while the relative error of the TNN method can also arrive at the accuracy of  $1 \times 10^{-8}$ .

**Table 6:** Errors of single-term time fractional Fredholm IDE for different values of  $\beta$  of AO-fPINNs, AWAO-fPINNs and  $e_{\text{test}}$  of TNNs with  $\mu = \beta$ .

$\beta$	AO-fPINNs [40]	AWAO-fPINNs [40]	TNNs
0.4	1.001e-3	6.825e-4	8.063e-08
0.6	1.047e-3	5.550e-4	4.415e-08

#### 4.2.2 Two-term TFPDE with weakly singular Fredholm integral

To demonstrate the adaptability of our method for solving TFPIDEs with weakly singular Fredholm integrals, we consider the following two-term TFPIDE: Find  $u(x, t)$  such that

$$\left\{ \begin{array}{l} \sum_{k=1}^2 {}_0^C D_t^{\beta_k} u(x, t) = \frac{\partial^2 u(x, t)}{\partial x^2} + f(x, t, u) \\ \quad + \int_0^1 |t-s|^{-1/2} u(x, s) ds, \quad (x, t) \in (0, 1) \times (0, 1], \\ f(x, t, u) = h(x, t) - u^2(x, t), \quad (x, t) \in [0, 1] \times (0, 1], \\ u(x, 0) = 0, \quad x \in [0, 1], \\ u(0, t) = u(1, t) = 0, \quad t \in (0, 1], \end{array} \right. \quad (4.6)$$

where  $\beta_1, \beta_2 \in (0, 1)$ .

For the weakly singular Fredholm integral in this example, we decompose it into two Volterra integrals as follows

$$\int_0^1 |t-s|^{-1/2} s^\mu \phi_{1,j}(s) ds = \int_t^1 (s-t)^{-1/2} s^\mu \phi_{1,j}(s) ds + \int_0^t (t-s)^{-1/2} s^\mu \phi_{1,j}(s) ds. \quad (4.7)$$

In order to transform the intervals of the above two integrals to  $[0, 1]$ , we perform the linear transformations of  $s = t + (1-t)m$  and  $s = tm$ . Then the integral (4.7) can be computed as follows

$$\begin{aligned} & \int_0^1 |t-s|^{-1/2} s^\mu \phi_{t,j}(s) ds \\ &= (1-t)^{1/2} \int_0^1 m^{-1/2} [t + (1-t)m]^\mu \phi_{t,j}(t + (1-t)m) dm \\ & \quad + t^{1-1/2+\mu} \int_0^1 (1-m)^{-1/2} m^\mu \phi_{t,j}(tm) dm \end{aligned}$$

$$\begin{aligned}
&= (1-t)^{1/2} \sum_{k=1}^{N_m} w_k^{(0,-1/2)} [t + (1-t)m_k^{(0,-1/2)}]^\mu \phi_{t,j}(t + (1-t)m_k^{(0,-1/2)}) \\
&\quad + t^{1/2+\mu} \sum_{k=1}^{N_m} w_k^{(-1/2,\mu)} \phi_{t,j}(tm_k^{(-1/2,2\mu)}).
\end{aligned}$$

Then the Fredholm integral in this example can be discretized as follows:

$$\int_0^1 |t-s|^{-1/2} \Psi(x, s) ds = \sum_{j=1}^p c_j \phi_{1,j}(x) \int_0^1 |t-s|^{-1/2} s^\mu \phi_{t,j}(s) ds.$$

We choose the source term

$$\begin{aligned}
f(x, t, u) &= \sum_{i=1}^2 \frac{\Gamma(3)}{\Gamma(3-\beta_i)} t^{2-\beta_i} \sin(2\pi x) + 2\pi^2 t^2 \sin(2\pi x) \\
&\quad - \left[ B(1/2, 3) t^{5/2} + 2(1-t)^{1/2} t^2 + \frac{4}{3}(1-t)^{3/2} t + \frac{2}{5}(1-t)^{5/2} \right] \sin(2\pi x),
\end{aligned}$$

where  $B(\cdot, \cdot)$  is the beta function. Then the exact solution to (4.6) is  $u(x, t) = t^2 \sin(2\pi x)$ .

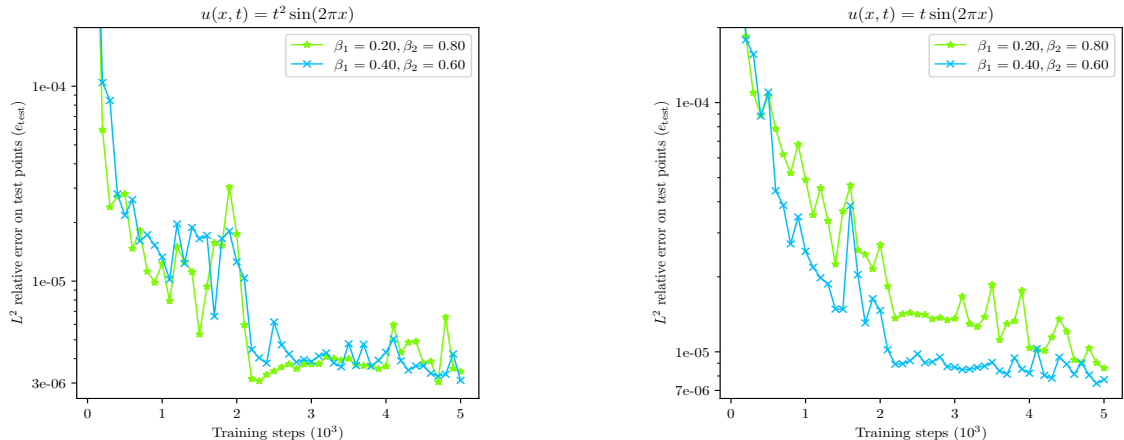


**Figure 10:** The relative  $L^2$  error during the training process for solving equation (4.6) with the exact solution  $u = t^2 \sin(2\pi x)$  (left) and  $u = t \sin(2\pi x)$  (right).

In addition, we set the source term as

$$f(x, t, u) = \left[ \sum_{i=1}^2 \frac{\Gamma(2)}{\Gamma(2-\beta_i)} t^{1-\beta_i} + 4\pi^2 t - B(1/2, 2) t^{3/2} - 2t(1-t)^{1/2} - \frac{2}{3}(1-t)^{3/2} \right] \sin(2\pi x),$$

such that the exact solution to (4.6) is  $u(x, t) = t \sin(2\pi x)$ .

The corresponding numerical results are shown in Figures 10 and 11, Table 7, which show that the relative error can reach the high accuracy of  $1 \times 10^{-6}$ .

### 4.3 Nonlinear TFPIDEs with Volterra integral

In this subsection, we focus on solving one- and three-dimensional single/multi-term nonlinear TFPIDEs (1.1) involving Volterra integrals.

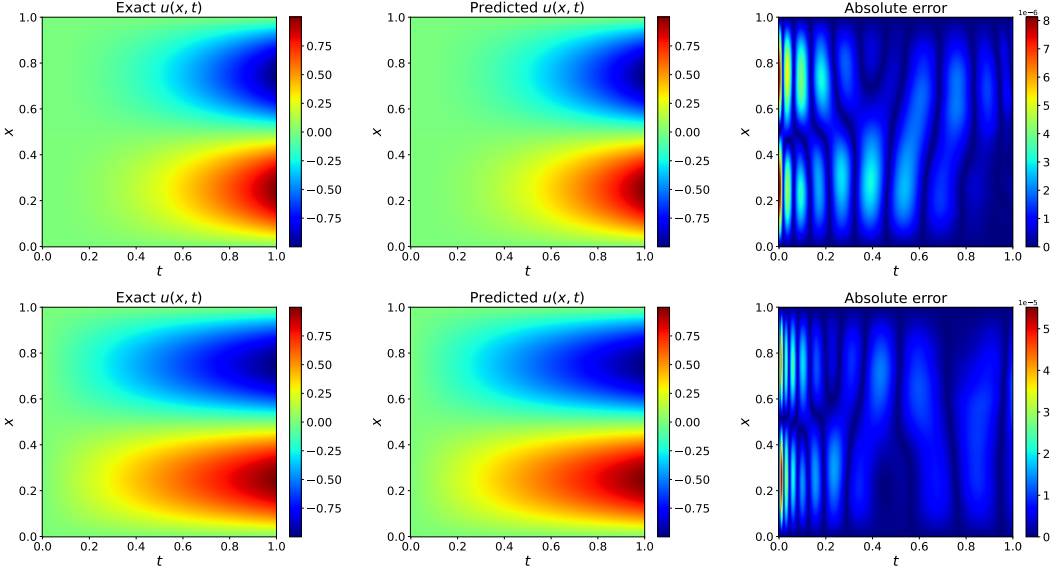


**Figure 11:** Numerical results of the two-term time-fractional diffusion wave equation with exact solutions  $u(x, t) = t^2 \sin(2\pi x)$  for  $\beta_1 = 0.20$ ,  $\beta_2 = 0.80$  (top row) and  $u(x, t) = t \sin(2\pi x)$  for  $\beta_1 = 0.20$ ,  $\beta_2 = 0.80$  (bottom row): the exact solutions (left column), the predictions (middle column), and the absolute errors of approximation (right column) ( $\mu = \beta_1$ ).

**Table 7:** Errors of two-term TFPIDE for different values of fractional order  $\beta_1, \beta_2 \in (0, 1)$  with  $\mu = \beta_1$  for  $u(x, t) = t^2 \sin(2\pi x)$  and  $u(x, t) = t \sin(2\pi x)$ .

$u(x, t) = t^2 \sin(2\pi x)$			$u(x, t) = t \sin(2\pi x)$		
$(\beta_1, \beta_2)$	$e_{L^2}$	$e_{\text{test}}$	$(\beta_1, \beta_2)$	$e_{L^2}$	$e_{\text{test}}$
(0.2, 0.8)	4.842e-06	4.801e-06	(0.2, 0.8)	1.035e-05	8.547e-06
(0.4, 0.6)	3.407e-06	3.290e-06	(0.4, 0.6)	8.549e-06	7.555e-06

#### 4.3.1 Single-term TFPIDE with double Volterra integrals

We consider the following nonlinear TFPIDE with non-homogeneous boundary conditions to validate the robustness of our method in solving TFPIDEs with non-homogeneous boundary conditions: Find  $u(x, t)$  such that

$$\left\{ \begin{array}{l} {}_0^C D_t^\beta u(x, t) = \frac{\partial^2 u(x, t)}{\partial x^2} + f(x, t, u) \\ \quad + \int_0^t \int_0^x \tau e^{x-s} u(s, \tau) ds d\tau, \quad (x, t) \in (0, 1) \times [0, 1], \\ f(x, t, u) = h(x, t) - u^2(x, t), \quad (x, t) \in [0, 1] \times (0, 1], \\ u(x, 0) = e^x, \quad x \in [0, 1], \\ u(0, t) = (t-1)^2, \quad u(1, t) = e(t-1)^2, \quad t \in (0, 1], \end{array} \right. \quad (4.8)$$

where  $\beta \in (0, 1)$ . The source term is set to be

$$\begin{aligned} f(x, t, u) = & e^x \left( \frac{2}{\Gamma(3-\beta)} t^{2-\beta} - \frac{2}{\Gamma(2-\beta)} t^{1-\beta} \right) - x e^x \left( \frac{1}{4} t^4 - \frac{2}{3} t^3 + \frac{1}{2} t^2 \right) \\ & + e^x (t-1)^2 (e^x (t-1)^2 - 1), \end{aligned}$$

such that the exact solution to (4.8) is  $u(x, t) = e^x (t-1)^2$ .

By using the mappings  $\tau = xn$  and  $s = tm$ , the interval of the Volterra integral is transformed to  $[0, 1]$  and then the Gauss-Jacobi quadrature scheme is used for computing double integral in (4.8) of the corresponding TNN approximation  $\Psi(x, t, c, \theta)$  as follows

$$\begin{aligned} \int_0^t \int_0^x \tau e^{x-s} \Psi(s, \tau) ds d\tau &= \int_0^1 tdm \int_0^1 tme^{x-xn} \Psi(xn, tm) xdn \\ &\approx \sum_{j=1}^p c_j \sum_{i=1}^{N_n} w_i^n e^{x(1-n_i)} x \phi_{1,j}(xn_i) \sum_{k=1}^{N_m} w_k^m m_k^{1+\mu} t^{2+\mu} \phi_{t,j}(tm_k), \end{aligned}$$

where  $\{w_i^n, n_i\}_{i=1}^{N_m}$  and  $\{w_k^m, m_k\}_{k=1}^{N_m}$  denote the weights and nodes of Gauss-Legendre quadrature scheme on the interval  $[0, 1]$ . This interval is subdivided into 25 subintervals, with 16 Gauss points selected within each subinterval to ensure sufficient accuracy for discretizing the Volterra integral.

We construct a new function  $\hat{g}(x, t) = [(e-1)x + 1](t-1)^2$  and equation (4.8) can be transformed into the one for the exact solution  $\hat{u}(x, t)$  with the homogeneous initial boundary value conditions by the following decomposition

$$u(x, t) = \hat{u}(x, t) + e^x - (e-1)x - 1 + \hat{g}(x, t).$$

During the training process, the corresponding numerical results are presented in Figures 12

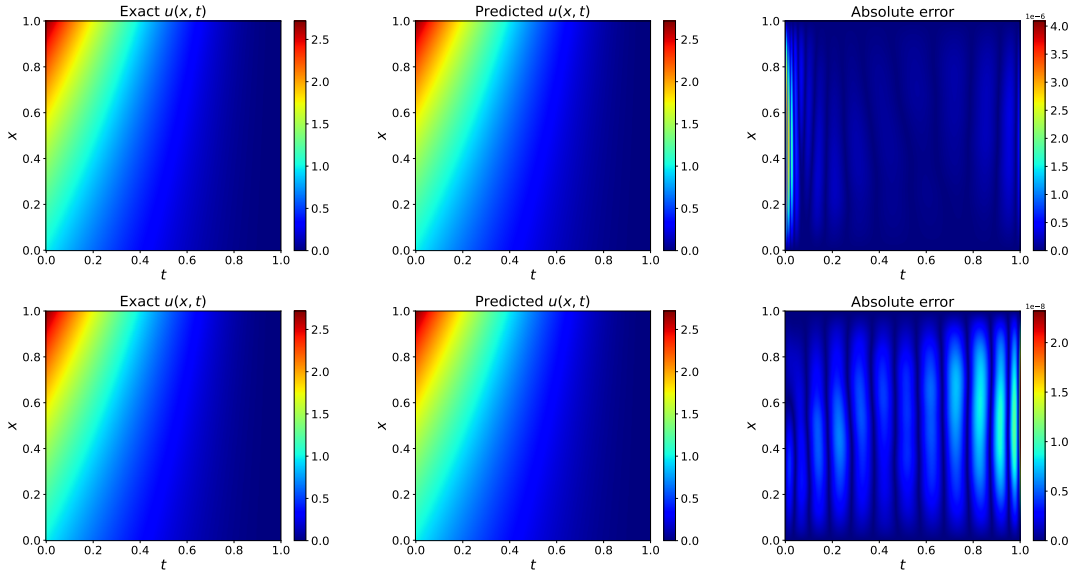


**Figure 12:** Numerical results of the nonlinear TFPIDE with double integrals for  $\beta = 0.20$  (top row) and  $\beta = 1$  (bottom row): the exact solutions (left column), the predictions (middle column), and the absolute errors of approximation (right column) ( $\mu = \beta$ ).

and 13, Table 8. These results demonstrate that the relative error can only achieve an accuracy of  $1 \times 10^{-7}$  when  $\mu = \beta$ , whereas it reaches a higher accuracy of  $1 \times 10^{-9}$  with  $\mu = 1$ . This discrepancy arises because the choice of  $\mu = \beta$  introduces certain singularities when solving equation (4.8). Nevertheless, even if the smoothness of the solution is unknown and  $\mu = \beta$  is selected, the relative error still attains a high accuracy of  $1 \times 10^{-7}$ , which is significantly superior to the accuracy achieved by AO-fPINNs and AWAO-fPINNs [40].

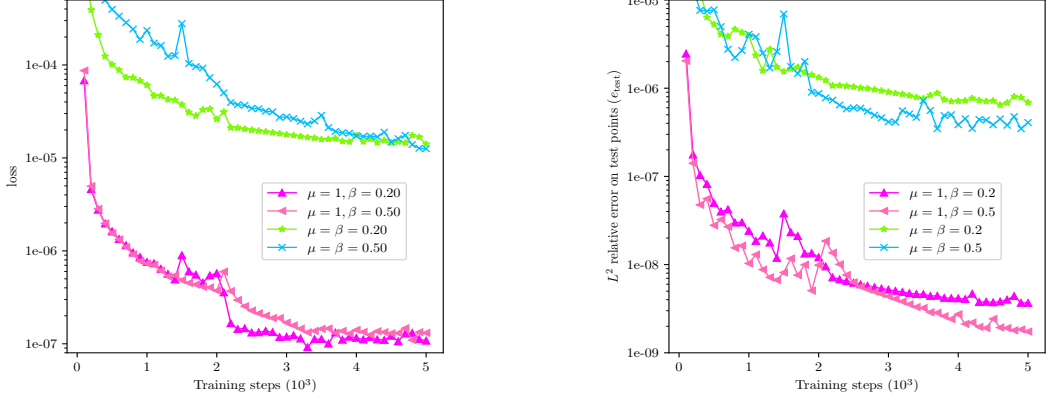


**Figure 13:** The loss curve and relative  $L^2$  error during the training process for solving equation (4.8).

**Table 8:** Errors of time fractional integro-differential equations for different values of  $\beta$  by AO-fPINNs, AWAO-fPINNs [40] and TNN method with  $\mu = \beta$

$\beta$	AO-fPINNs	AWAO-fPINNs	TNNs ( $\mu = \beta$ )	TNNs ( $\mu = 1$ )
0.2	1.503e-3	5.599e-4	6.582e-07	2.783e-09
0.5	9.265e-4	2.455e-4	3.486e-07	1.844e-09

#### 4.3.2 Three-term mixed-order time-fractional Volterra IDE

To validate the effectiveness of the proposed TNN method in solving mixed-order nonlinear TFPIDE, we consider the following three-term nonlinear TFPIDE with fractional orders  $0 < \beta_1 < 1 < \beta_2 < \beta_3 < 2$ : Find  $u(x, t)$  such that

$$\left\{ \begin{array}{l} \sum_{k=1}^3 {}_0^C D_t^{\beta_k} u(x, t) = \frac{\partial^2 u(x, t)}{\partial x^2} + f(x, t, u) \\ \quad + \int_0^t \cos(\tau - x) u(x, \tau) d\tau, \quad (x, t) \in [0, 1] \times (0, 1], \\ f(x, t, u) = h(x, t) - u^2(x, t), \quad (x, t) \in [0, 1] \times (0, 1], \\ u(0, t) = 0, u(1, t) = 0, \quad t \in (0, 1], \\ u(x, 0) = \sin(\pi x), \quad x \in [0, 1]. \end{array} \right. \quad (4.9)$$

The exact solution to (4.9) is set to be  $u(x, t) = (t^3 + 1) \sin(\pi x)$  and then the source term should be

$$\begin{aligned} f(x, t, u) = & \sum_{i=1}^3 \frac{6}{\Gamma(4 - \beta_i)} t^{3 - \beta_i} \sin(\pi x) + \pi^2 (t^3 + 1) \sin(\pi x) \\ & - \sin(\pi x) [(t^3 - 6t + 1) \sin(t - x) + (3t^2 - 6) \cos(t - x) + \sin(x) + 6 \cos(x)]. \end{aligned}$$

To transform the intervals of the Volterra integral to  $[0, 1]$ , we perform a linear transformation of  $\tau = tm$  and the Gauss-Legendre quadrature is used for computing the integral as follows

$$\int_0^t \cos(\tau - x) \Psi(x, \tau) d\tau = \int_0^1 \cos(tm - x) \Psi(x, tm) t dm$$

$$\begin{aligned}
&\approx \sum_{j=1}^p c_j \phi_{1,j}(x) \cos(x) \sum_{k=1}^{N_m} w_k \cos(tm_k) t^2 m_k \phi_{t,j}(tm_k) \\
&+ \sum_{j=1}^p c_j \phi_{1,j}(x) \sin(x) \sum_{k=1}^{N_m} w_k \sin(tm_k) t^2 m_k \phi_{t,j}(tm_k),
\end{aligned}$$

where  $\{w_k, m_k\}_{k=1}^{N_m}$  denote the nodes and weights of Gauss-Legendre quadrature in interval  $[0, 1]$ . This interval is subdivided into 25 subintervals, with 16 Gauss points selected within each subinterval to ensure sufficient accuracy for discretizing the integral.

By the decomposition  $u(x, t) = \hat{u}(x, t) + \sin(\pi x)$ , we can transform equation (4.9) into a homogeneous initial value PDE with the exact solution  $\hat{u}(x, t)$ . The corresponding numerical

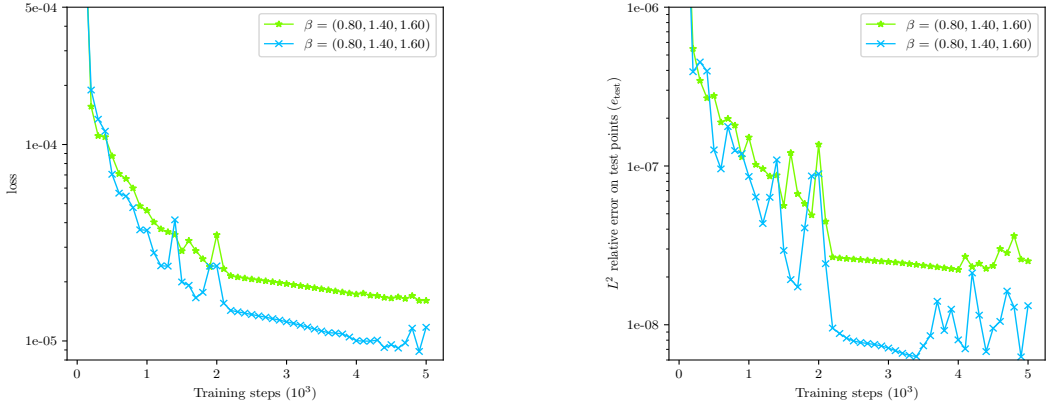


**Figure 14:** The loss curve and relative  $L^2$  error during the training process for solving equation (4.9).

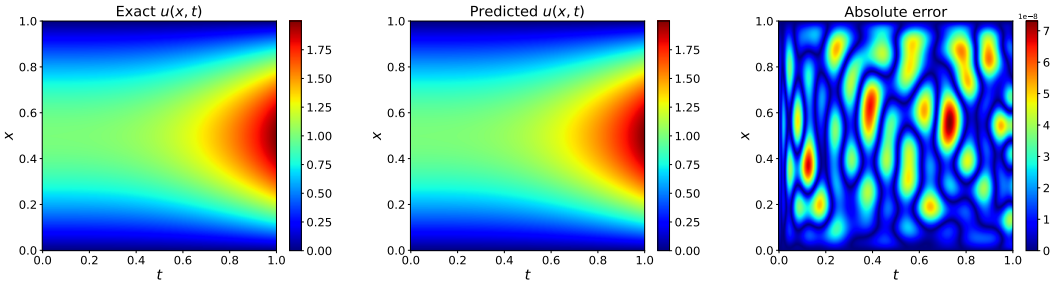


**Figure 15:** Numerical results for three-term mixed-order TFPIDE with Volterra integral for  $\beta_1 = 0.8, \beta_2 = 1.4, \beta_3 = 1.6$ : the exact solution (left), the prediction (middle), and the absolute errors (right) with  $\mu = \beta_2$ .

results are shown in Figure 14 and 15, Table 9, which demonstrate that the relative error of the TNN method proposed in this paper can reach  $1 \times 10^{-9}$ , while the relative errors of AO-fPINNs and AWAO-fPINNs are only around  $1 \times 10^{-4}$ . This highlights the superior capability of the TNN method to achieve high-precision numerical solutions for equation (4.9).

**Table 9:** Errors of three-term nonlinear TFPIDE for different values of  $\beta_1, \beta_2, \beta_3$  of AO-fPINNs, AWAO-fPINNs and of TNNs with  $u(x, t) = (t^3 + 1) \sin(x)$  and  $\mu = \beta_2$ .

$\beta = (\beta_1, \beta_2, \beta_3)$	AO-fPINNs [40]	AWAO-fPINNs [40]	TNNs
(0.8,1.4,1.6)	1.582e-3	2.675e-4	2.438e-08
(0.5,1.5,1.9)	1.183e-3	4.535e-4	9.236e-09

#### 4.3.3 3D time-fractional IDE with quadruple Volterra integrals

Here, we consider the following three-dimensional time-fractional IDE with quadruple integrals and fractional order  $\beta_1, \beta_2 \in (1, 2)$ : Find  $u(x, t)$  such that

$$\left\{ \begin{array}{l} \sum_{k=1}^2 {}_0^C D_t^{\beta_k} u(\mathbf{x}, t) = \Delta u(\mathbf{x}, t) + f(\mathbf{x}, t, u) + v(\mathbf{x}, t, u), (\mathbf{x}, t) \in \Omega \times (0, T], \\ v(\mathbf{x}, t, u) = \int_0^t \int_0^{x_3} \int_0^{x_2} \int_0^{x_1} \tau(p-q)u(p, q, s, \tau) dp dq ds d\tau, \\ f(\mathbf{x}, t, u) = h(\mathbf{x}, t) - u^2(\mathbf{x}, t), (\mathbf{x}, t) \in \Omega \times (0, T], \\ u(\mathbf{x}, t) = 0, \mathbf{x} \in \partial\Omega, t \in (0, T], \\ u(\mathbf{x}, 0) = 0, \mathbf{x} \in \bar{\Omega}, \end{array} \right. \quad (4.10)$$

For the first example, we consider the domain  $\Omega = (0, \pi)^3$ , the time interval  $T = 1$ , and the exact solution to (4.10) as  $u(\mathbf{x}, t) = t^{2+\beta_2} \prod_{i=1}^3 \sin(\pi x_i)$  by setting the source term as

$$f(\mathbf{x}, t, u) = \prod_{i=1}^3 \sin(\pi x_i) \left[ \sum_{k=1}^2 \frac{\Gamma(3 + \beta_2)}{\Gamma(3 + \beta_2 - \beta_k)} t^{2+\beta_2-\beta_k} \right] + \frac{t^{4+\beta_2}}{4 + \beta_2} (\cos(x_3) - 1) I(x_1, x_2),$$

where the function  $I(x, y) := \sin(y-x) + \sin(x) - \sin(y) + (x-y) \cos(x) \cos(y) + y \cos(y) - x \cos(x)$ .

For the second example, we consider the domain  $\Omega = (0, 1)^3$ , the time interval  $T = 1$ , and choose the non-variable-separated exact solution to (4.10) as  $u(\mathbf{x}, t) = t^{2\beta_2} e^{x_1 x_2 x_3} \prod_{i=1}^3 \sin(\pi x_i)$ . The source term can be obtained from the exact solution as

$$\begin{aligned} & f(\mathbf{x}, t, u) \\ &= e^{x_1 x_2 x_3} \prod_{i=1}^3 \sin(\pi x_i) \left[ \sum_{k=1}^2 \frac{\Gamma(2\beta_2 + 1)}{\Gamma(2\beta_2 + 1 - \beta_k)} t^{2\beta_2 - \beta_k} - ((x_2 x_3)^2 + (x_1 x_3)^2 + (x_1 x_2)^2 - 3\pi^2) t^{2\beta_2} \right] \\ & \quad - 2\pi t^{2\beta_2} e^{x_1 x_2 x_3} [\cos(\pi x_1) J(x_2, x_3) + \cos(\pi x_2) J(x_1, x_3) + \cos(\pi x_3) J(x_1, x_2)] \\ & \quad - \frac{t^{2\beta_2 + 2} x_1 x_2 x_3}{2(\beta_2 + 1)} \int_0^1 \int_0^1 \int_0^1 (x_1 m - x_2 n) e^{x_1 x_2 x_3 m n h} \sin(\pi x_1 m) \sin(\pi x_2 n) \sin(\pi x_3 h) dm dn dh, \end{aligned}$$

where the function  $J(x, y) =: xy \sin(\pi x) \sin(\pi y)$ .

The domain of the quadruple Volterra integrals can be transformed into the unit hypercube  $[0, 1]^4$  by applying the linear mappings  $p = x_1 m$ ,  $q = x_2 n$ ,  $s = x_3 h$ , and  $\tau = t\eta$ . Then the Gauss-Legendre quadrature on the interval  $[0, 1]$  can be used for computing the Volterra integral as follows

$$\begin{aligned} & v(\mathbf{x}, t, \Psi) \\ & \approx \sum_{j=1}^p c_j \sum_{s=1}^{N_m} w_s x_1^2 m_s \phi_{1,j}(x_1 m_s) \sum_{\iota=1}^{N_n} w_\iota x_2 \phi_{2,j}(x_2 n_\iota) \sum_{r=1}^{N_h} w_r x_3 \phi_{3,j}(x_3 h_r) \sum_{k=1}^{N_\eta} w_k \eta_k^{1+\mu} t^{2+\mu} \phi_{t,j}(t \eta_k) \end{aligned}$$

$$-\sum_{j=1}^p c_j \sum_{s=1}^{N_m} w_s x_1 \phi_{1,j}(x_1 m_s) \sum_{\iota=1}^{N_n} w_\iota x_2^2 n_\iota \phi_{2,j}(x_2 n_\iota) \sum_{r=1}^{N_h} w_r x_3 \phi_{3,j}(x_3 h_r) \sum_{k=1}^{N_\eta} w_k \eta_k^{1+\mu} t^{2+\mu} \phi_{t,j}(t \eta_k),$$

where  $\{w_s, m_s\}_{s=1}^{N_m}$ ,  $\{w_\iota, m_\iota\}_{\iota=1}^{N_n}$ ,  $\{w_r, m_r\}_{r=1}^{N_h}$  and  $\{w_k, m_k\}_{k=1}^{N_\eta}$  denote the nodes and weights of the Gauss-Legendre quadrature on the interval  $[0, 1]$ . This interval is divided into 10 subintervals, with 16 Gauss points selected within each subinterval to ensure sufficient accuracy for discretizing the quadruple Volterra integrals.

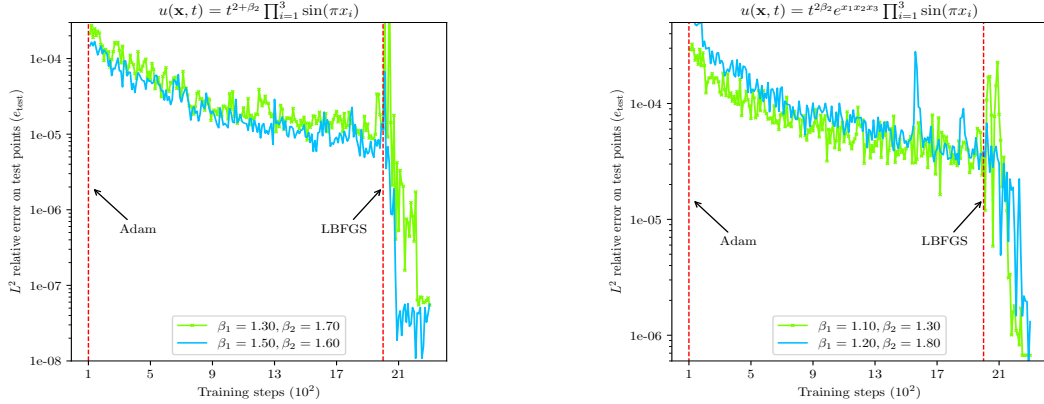


**Figure 16:** The loss curve and relative  $L^2$  error during the training process for solving equation (4.10) with different exact solutions.

**Table 10:** Errors of TFPIDE with quadruple Volterra integrals for different values of fractional order  $\beta_1, \beta_2 \in (1, 2)$  with  $\mu = \beta_1$ .

$u(\mathbf{x}, t) = t^{2+\beta_2} \prod_{i=1}^3 \sin(\pi x_i)$	$u(\mathbf{x}, t) = t^{2\beta_2} e^{x_1 x_2 x_3} \prod_{i=1}^3 \sin(\pi x_i)$		
$(\beta_1, \beta_2)$	$e_{\text{test}}$	$(\beta_1, \beta_2)$	$e_{\text{test}}$
(1.30, 1.70)	5.496e-08	(1.10, 1.30)	6.719e-07
(1.50, 1.60)	3.758e-08	(1.20, 1.80)	8.306e-07

During the training process. The TNN is optimized using the Adam optimizer with an initial learning rate of 0.003 for the 2000 epochs, followed by the LBFGS optimizer with a learning rate of 0.1 for 300 steps to obtain the final result. The corresponding numerical results are shown in Figure 16 and Table 10, indicate that the relative error for choosing  $\mu = \beta_1$  is exceptionally high, reaching up to about  $1 \times 10^{-7}$ . This also indicates that the TNN method proposed in this article can accurately solve similar high-dimensional problems.

## 5 Conclusion

In this paper, inspired by the concept of subspace approximation from the FEM and TNN for high dimensional problems, we propose an adaptive TNN subspace-based machine learning method for solving linear and nonlinear TFPIDEs with high accuracy. Specifically, we design the TNN function multiplied by the factor function  $t^\mu$ , which efficiently combines Gauss-Jacobi quadrature to solve TFPIDEs (1.1) with high accuracy. The proposed TNN-based machine learning method demonstrates superior performance compared to FPINN and its variants, achieving significant improvements in both accuracy and computational efficiency.

In the future, we will consider the TNN-based machine learning method for solving other

types of Fredholm or Volterra integral equations and spatial fractional partial differential equations.

## References

- [1] Mohd Rashid Admon, Norazak Senu, Ali Ahmadian, Zanariah Abdul Majid, and Soheil Salahshour. A new efficient algorithm based on feedforward neural network for solving differential equations of fractional order. *Commun. Nonlinear Sci. Numer. Simul.*, 117:106968, 2023.
- [2] D. W. Brzezinski. Computation of Gauss-Jacobi quadrature nodes and weights with arbitrary precision. In *Proc. FedCSIS*, pages 297–306. IEEE, 2018.
- [3] Mehdi Dehghan, Mostafa Abbaszadeh, and Akbar Mohebbi. Legendre spectral element method for solving time fractional modified anomalous sub-diffusion equation. *Appl. Math. Model.*, 40(5-6):3635–3654, 2016.
- [4] S. Harizanov, R. Lazarov, and S. Margenov. A survey on numerical methods for spectral space-fractional diffusion problems. *Fract. Calc. Appl. Anal.*, 23(6):1605–1646, 2020.
- [5] Zheyuan Hu, Khemraj Shukla, George Em Karniadakis, and Kenji Kawaguchi. Tackling the curse of dimensionality with physics-informed neural networks. *Neural Networks*, 176:106369, Aug 2024.
- [6] Jianfei Huang, Yifa Tang, Luis Vázquez, and Jiye Yang. Two finite difference schemes for time fractional diffusion-wave equation. *Numer. Algorithms*, 64:707–720, 2013.
- [7] Hossein Jafari, Sohrab Ali Yousefi, MA Firoozjaee, Shaher Momani, and Chaudry Masood Khalique. Application of Legendre wavelets for solving fractional differential equations. *Comput. Math. Appl.*, 62(3):1038–1045, 2011.
- [8] Salman Jahanshahi, Esmail Babolian, Delfim FM Torres, and AR Vahidi. A fractional Gauss-Jacobi quadrature rule for approximating fractional integrals and derivatives. *Chaos Solitons Fractals*, 102:295–304, 2017.
- [9] Shidong Jiang, Jiwei Zhang, Qian Zhang, and Zhimin Zhang. Fast evaluation of the Caputo fractional derivative and its applications to fractional diffusion equations. *Commun. Comput. Phys.*, 21(3):650–678, 2017.
- [10] Yingjun Jiang and Jingtang Ma. High-order finite element methods for time-fractional partial differential equations. *J. Comput. Appl. Math.*, 235(11):3285–3290, 2011.
- [11] Bangti Jin, Buyang Li, and Zhi Zhou. Subdiffusion with a time-dependent coefficient: analysis and numerical solution. *Math. Comp.*, 88(319):2157–2186, 2019.
- [12] Tunan Kao, He Zhang, Lei Zhang, and Jin Zhao. pETNNs: partial evolutionary tensor neural networks for solving time-dependent partial differential equations. *arXiv:2403.06084*, 2024.
- [13] Sarita Kumari and Rajesh K Pandey. Single-term and multi-term nonuniform time-stepping approximation methods for two-dimensional time-fractional diffusion-wave equation. *Comput. Math. Appl.*, 151:359–383, 2023.

- [14] Isaac E Lagaris, Aristidis Likas, and Dimitrios I Fotiadis. Artificial neural networks for solving ordinary and partial differential equations. *IEEE Trans. Neural Netw.*, 9(5):987–1000, 1998.
- [15] Yongxin Li, Zhongshuo Lin, Yifan Wang, and Hehu Xie. Tensor neural network interpolation and its applications. *arXiv:2404.07805*, 2024.
- [16] Yangfei Liao, Zhongshuo Lin, Jianghao Liu, Qingyuan Sun, Yifan Wang, Teng Wu, and Hehu Xie. Solving Schrödinger equation using tensor neural network. *arXiv:2209.12572*, 2022.
- [17] Luchang Ma, Rui Li, Fanhai Zeng, Ling Guo, and George Em Karniadakis. Bi-orthogonal fpinn: a physics-informed neural network method for solving time-dependent stochastic fractional pdes. *Commun. Comput. Phys.*, 34(4):1133–1176, 2023.
- [18] Zhiying Ma, Jie Hou, Wenhao Zhu, Yixin Peng, and Ying Li. PMNN: Physical model-driven neural network for solving time-fractional differential equations. *Chaos Solitons Fractals*, 177:114238, 2023.
- [19] Fakhrodin Mohammadi and Carlo Cattani. A generalized fractional-order Legendre wavelet tau method for solving fractional differential equations. *J. Comput. Appl. Math.*, 339:306–316, 2018.
- [20] Shaher Momani and Zaid Odibat. Analytical solution of a time-fractional Navier–Stokes equation by Adomian decomposition method. *Appl. Math. Comput.*, 177(2):488–494, 2006.
- [21] Shaher Momani and Zaid Odibat. Numerical approach to differential equations of fractional order. *J. Comput. Appl. Math.*, 207(1):96–110, 2007.
- [22] Guofei Pang, Lu Lu, and George Em Karniadakis. fPINNs: Fractional physics-informed neural networks. *SIAM J. Sci. Comput.*, 41(4):A2603–A2626, 2019.
- [23] Maziar Raissi, Paris Perdikaris, and George E Karniadakis. Physics-informed neural networks: A deep learning framework for solving forward and inverse problems involving nonlinear partial differential equations. *J. Comput. Phys.*, 378:686–707, 2019.
- [24] S Saha Ray and RK Bera. An approximate solution of a nonlinear fractional differential equation by Adomian decomposition method. *Appl. Math. Comput.*, 167(1):561–571, 2005.
- [25] Hongpeng Ren, Xiangyun Meng, Rongrong Liu, Jian Hou, and Yongguang Yu. A class of improved fractional physics informed neural networks. *Neurocomputing*, 562:126890, 2023.
- [26] S Salahshour, T Allahviranloo, and S Abbasbandy. Solving fuzzy fractional differential equations by fuzzy Laplace transforms. *Commun. Nonlinear Sci. Numer. Simul.*, 17(3):1372–1381, 2012.
- [27] Mianfu She, Dongfang Li, and Hai-wei Sun. A transformed L1 method for solving the multi-term time-fractional diffusion problem. *Math. Comput. Simul.*, 193:584–606, 2022.
- [28] V Srivastava and KN Rai. A multi-term fractional diffusion equation for oxygen delivery through a capillary to tissues. *Math. Comput. Model.*, 51(5-6):616–624, 2010.
- [29] Zhi-Zhong Sun and Guang-hua Gao. *Fractional differential equations: finite difference methods*. De Gruyter, 2020.

[30] Younes Talaei and MJNC Asgari. An operational matrix based on Chelyshkov polynomials for solving multi-order fractional differential equations. *Neural Comput. Appl.*, 30:1369–1376, 2018.

[31] Peter J Torvik and Ronald L Bagley. On the appearance of the fractional derivative in the behavior of real materials. *J. Appl. Mech.*, 51(2):294–298, 1984.

[32] Shupeng Wang and George Em Karniadakis. GMC-PINNs: A new general Monte Carlo PINNs method for solving fractional partial differential equations on irregular domains. *Comput. Methods Appl. Mech. Eng.*, 429:117189, 2024.

[33] Taorui Wang, Zheyuan Hu, Kenji Kawaguchi, Zhongqiang Zhang, and George Em Karniadakis. Tensor neural networks for high-dimensional Fokker-Planck equations. *Neural Netw.*, page 107165, 2025.

[34] Yifan Wang, Pengzhan Jin, and Hehu Xie. Tensor neural network and its numerical integration. *ArXiv:2207.02754*, 2022.

[35] Yifan Wang, Zhongshuo Lin, Yangfei Liao, Haochen Liu, and Hehu Xie. Solving high-dimensional partial differential equations using tensor neural network and a posteriori error estimators. *J. Sci. Comput.*, 101(3):1–29, 2024.

[36] Yifan Wang and Hehu Xie. Computing multi-eigenpairs of high-dimensional eigenvalue problems using tensor neural networks. *J. Comput. Phys.*, 506:112928, 2024.

[37] Zhaodong Xu and Zhiqiang Sheng. Subspace method based on neural networks for solving the partial differential equation. *arXiv:2404.08223*, 2024.

[38] Fanhai Zeng, Zhongqiang Zhang, and George Em. Karniadakis. Second-order numerical methods for multi-term fractional differential equations: smooth and non-smooth solutions. *Comput. Methods Appl. Mech. Eng.*, 327:478–502, 2017.

[39] Hui Zhang, Fanhai Zeng, Xiaoyun Jiang, and Zhimin Zhang. Fast time-stepping discontinuous Galerkin method for the subdiffusion equation. *IMA J. Numer. Anal.*, page drae087, 2024.

[40] Jingna Zhang, Yue Zhao, and Yifa Tang. Adaptive loss weighting auxiliary output fPINNs for solving fractional partial integro-differential equations. *Physica D*, 460:134066, 2024.

[41] Tianxin Zhang, Dazhi Zhang, Shengzhu Shi, and Zhichang Guo. Spectral-fPINNs: spectral method based fractional physics-informed neural networks for solving fractional partial differential equations. *Nonlinear Dyn.*, pages 1–24, 2025.

[42] Yue Zhao, Weiping Bu, Xuan Zhao, and Yifa Tang. Galerkin finite element method for two-dimensional space and time fractional Bloch–Torrey equation. *J. Comput. Phys.*, 350:117–135, 2017.